IMPROVED RANGE ESTIMATION USING SIMPLE INFRARED SENSORS WITHOUT PRIOR KNOWLEDGE OF SURFACE CHARACTERISTICS

A THESIS

SUBMITTED TO THE DEPARTMENT OF ELECTRICAL AND

ELECTRONICS ENGINEERING

AND THE INSTITUTE OF ENGINEERING AND SCIENCE

OF BİLKENT UNIVERSITY

IN PARTIAL FULFILLMENT OF THE REQUIREMENTS

FOR THE DEGREE OF

MASTER OF SCIENCE

By

R. Çağrı Yüzbaşıoğlu

September 2004

I certify that I have read this thesis and that in my opinion it is fully adequate, in scope and in quality, as a thesis for the degree of Master of Science.

Prof. Dr. Billur Barshan (Supervisor)

I certify that I have read this thesis and that in my opinion it is fully adequate, in scope and in quality, as a thesis for the degree of Master of Science.

Prof. Dr. Ömer Morgül

I certify that I have read this thesis and that in my opinion it is fully adequate, in scope and in quality, as a thesis for the degree of Master of Science.

Asst. Prof. Dr. Erol Şahin

Approved for the Institute of Engineering and Science:

Prof. Dr. Mehmet B. Baray
Director of the Institute Engineering and Science

ABSTRACT

IMPROVED RANGE ESTIMATION USING SIMPLE INFRARED SENSORS WITHOUT PRIOR KNOWLEDGE OF SURFACE CHARACTERISTICS

R. Çağrı Yüzbaşıoğlu
M.S. in Electrical and Electronics Engineering
Supervisor: Prof. Dr. Billur Barshan
September 2004

This thesis describes a new method for range estimation using low-cost infrared sensors. The intensity data acquired with infrared sensors depends highly on the surface properties and the configuration of the sensors with respect to the surface. Therefore, in many related studies, either the properties of the surface are determined first or certain assumptions about the surface are made in order to estimate the distance and the orientation of the surface relative to the sensors. We propose a novel method for position estimation of surfaces with infrared sensors without the need to determine the surface properties first. The method is relatively independent of the type of surface encountered since it is based on searching the maximum value of the intensity rather than using absolute intensity values for a given surface which would depend on the surface type. The method is verified experimentally with planar surfaces of different surface properties. An intelligent feature of our system is that its operating range is made adaptive based on the intensity of the detected signal. Three different ways of processing the intensity signals are considered for range estimation. The overall absolute mean error in the range estimates has been calculated as 0.15 cm in the range from 10 to 50 cm. The cases where the azimuth and elevation angles are nonzero are considered as well. The results obtained demonstrate that infrared sensors can be used for localization to an unexpectedly high accuracy without prior knowledge of the surface characteristics.

Keywords: infrared sensors, Phong illumination model, range estimation, surface localization, optical sensing.

ÖZET

KIZILBERİSİ ALGILAYICILARDAN ELDE EDİLEN SİNYALLERLE YÜZEY ÖZELLİKLERİNDEN BAĞIMSIZ UZAKLIK KESTİRİMİ

R. Çağrı Yüzbaşıoğlu
Elektrik ve Elektronik Mühendisliği, Yüksek Lisans
Tez Yöneticisi: Prof. Dr. Billur Barshan
Eylül 2004

Bu tezde, düşük maliyetli kızılberisi algılayıcılarla uzaklık kestirimi için yeni bir yöntem ileri sürülmektedir. Bu tip algılayıcılardan elde edilen yeğinlik ölçümleri büyük ölçüde yüzeyin özelliklerine ve algılayıcılara göre olan konumuna bağlıdır. Bu nedenle, kızılberisi algılayıcılarla yapılan önceki çalışmalarda, yüzeylerin konum kestirimi için öncelikle yüzey özellikleri çıkarılmakta veya yüzeyle ilgili bazı varsayımlarda bulunulmaktadır. Bu çalışma ise yüzey özelliklerine gerek duymaksızın, konum kestirimi için yeni bir yöntem ileri sürmektedir. Önerilen yöntem, yüzey özelliklerine bağlı olan mutlak yeğinlik değerlerini kullanmak yerine en büyük yeğinlik değerinin yerini bulmaya dayalı olduğundan, yüzey tipinden göreceli olarak bağımsızdır. Önerilen yöntem, farklı özelliklere sahip düzlemsel yüzeyler kullanılarak deneysel olarak doğrulanmıştır. Deneysel çalışmalarda kullandığımız sistemimizin akıllı bir özelliği çalışma alanının ölçülen yeğinlik değerlerine bağlı olarak kendiliğinden ayarlanabilmesidir. Uzaklık kestirimi için, yeğinlik ölçümleri üç farklı yöntemle işlenmektedir. 10–50 cm arasına yerleştirilen yüzeylerin konum kestiriminde, ortalama mutlak hata 0.15 cm olarak gerçekleşmiştir. Konum ve bakış açılarının sıfırdan farklı olduğu durumlar da incelenmiştir. Elde edilen sonuçlar göstermektedir ki, kızılberisi algılayıcılar, önerilen yöntemle özellikleri bilinmeyen bir yüzeyin yüksek doğrulukla konum kestiriminde kullanılabilirler.

Anahtar sözcükler: kızılberisi algılayıcılar, Phong aydınlanma modeli, uzaklık kestirimi, yüzey konumlandırma, optik algılama.

Acknowledgment

I would like to express my gratitude to my supervisor Prof. Dr. Billur Barshan for her guidance, support, and encouragement throughout the development of this thesis.

I would like to express my special thanks and gratitude to Prof. Dr. Ömer Morgül and Asst. Prof. Dr. Erol Şahin for showing keen interest in the subject matter and accepting to read and review the thesis.

I would also like to thank Tayfun Aytaç for his unique and friendly help.

Contents

List of Figures

List of Tables

Chapter 1

INTRODUCTION

Sensing the environment is essential for intelligent robots. Ultrasonic and infrared sensors are commonly used and relatively low-cost sensing modalities to perform this task [1]. Infrared sensors may be preferable to ultrasonic sensors due to their narrower beamwidth and have a wide variety of applications in safety and security systems, process control, robotics and automation and remote sensing. Infrared sensors are used in pattern recognition for tasks such as face identification [2], automatic target recognition [3], target tracking [4], automatic vehicle detection [5], remote sensing [6], detection and identification of targets in background clutter [7, 8], and automated terrain analysis [9].

Other studies using infrared sensors include simple object and proximity detection, counting [10, 11], distance and depth monitoring [12], floor sensing, position control [13], obstacle/collision avoidance, and machine vision systems [14]. Infrared sensors are used in door detection [15], mapping of openings in walls [16], as well as monitoring doors/windows of buildings and vehicles, and as "light curtains" for protecting an area. In [17], an automated guided vehicle detects unknown obstacles by means of an "electronic stick" consisting of infrared sensors, using a strategy similar to that adopted by a blind person. Other researchers have dealt with the fusion of information from infrared and sonar sensors [18, 19] and infrared and radar systems [20, 21].

Infrared sensors are also widely used in robotics. In [22], infrared proximity sensing for a robot arm is discussed. Following this work, [23] describes a robot arm completely covered with an infrared skin sensor to detect nearby objects. In another study [24], the properties of a planar surface at a known distance have been determined using the Phong illumination model [25], and using this information, the infrared sensor employed has been modeled as an accurate range finder for surfaces over the range 5 to 23 cm. The greatest error over the range 10 to 16 cm has been calculated as 0.2 cm, whereas for the ranges lower than 10 cm the error incraesed to 0.5-0.6 cm. Reference [26] also deals with determining the range of a planar surface. By incorporating the optimal amount of additive noise in the infrared range measurement system, the authors were able to improve the system sensitivity and extend the operating range of the system. A number of commercially available infrared sensors are evaluated in [27] for space applications. References [28, 29] describe a passive infrared sensing system which identifies the locations of the people in a room. Infrared sensors have also been used for automated sorting of waste objects made of different materials [30, 31].

Typically, infrared sensors are used as a pair, one as an emitter and the other as a detector. The emitted light reflected from the target is detected by the detector. The intensity of the light detected depends on several parameters including mainly the surface properties and the relative orientation of the emitter, the detector, and the target. Therefore, the intensity data is often not reliable enough to make sufficiently accurate range estimates. One way to overcome this problem is to first determine the surface parameters [24, 32]. In [32], the range errors have reached to a few cm over the range 20 cm to 100 cm. Alternatively, template-based [33] and rule-based approaches [34] can be used to differentiate objects of different geometries. In [35], surfaces of the same geometry but made of different materials are differentiated with an approach similar to that used in [33]. Another approach to the problem, taken in this study, is to configure the emitter and the detector to reduce the number of parameters involved.

In this study, we use a pair of sensors (Figure 1.1), one as emitter, and the other as detector. The emitter and the detector are mounted on a vertical linear platform on which they can be moved independently along a straight line as

shown in Figure 1.2. Both sensors make a predetermined angle(γ) with the linear platform on which they slide. The reason that the linear platform stands vertically and not horizontally is that in many typical indoor environments, there is much less variation in depth in the vertical direction when compared to the horizontal, and this eliminates some complications in range estimation. The basic idea of our method is that, while the sensors are being moved, the detector reading is maximum at some positions and the corresponding positional values of the sensors can be used for range estimation with suitable processing of the infrared intensity signals. To realize this idea, the detector slides along the platform to collect intensity data and these data are compared to find the maximum in magnitude, for a given position of the emitter. The position of the detector, corresponding to the maximum intensity data, is recorded together with the corresponding *baseline separation,* which is the distance between the emitter and the detector. The distance to the surface is then estimated based on this information in a way which is relatively independent of surface type, as will be explained in more detail in Section 2. The system can be viewed as a triangulation system tuned for maximum intensity data. Since the method is based on searching the maximum value of the intensity rather than using absolute intensity values for a given surface which would depend on the surface type, it is relatively independent of the type of surface encountered. As long as intensity data are available over a given range of detector positions, range is estimated relatively independently of surface type. This is the main difference of our approach from the earlier attempts to estimate range with infrared sensors where the highest accuracy achieved is 0.25 cm in the range from 10 to 20 cm.

The organization of this thesis is as follows: in Chapter 2, the range estimation technique proposed in this study is described in detail. Experimental verification is presented in Chapter 3 where details of the experimental setup and experimental results under different conditions are provided. Three different ways of processing the infrared intensity signals are considered and evaluated. In the final chapter, conclusions are drawn and directions for future research are indicated.

Figure 1.1: A closeup view of the infrared sensor.

Figure 1.2: The experimental setup used in this study.

Chapter 2

POSITION ESTIMATION

The method presented in this study is based on the Phong Illumination Model [25], which is frequently used in computer graphics applications. This model combines the three types of reflection, which are ambient, diffuse, and specular reflection, in a single formula:

$$I = I_a k_a + I_i[k_d(\vec{\boldsymbol{l}}.\vec{\boldsymbol{n}})] + I_i[k_s(\vec{\boldsymbol{t}}.\vec{\boldsymbol{v}})^m] \tag{2.1}$$

Here, I_a and I_i are the intensities of ambient and incident light, k_a, k_d, and k_s are the coefficients of ambient, diffuse, and specular reflections for a given material, m is the specular fall-off factor, and $\vec{\boldsymbol{l}}, \vec{\boldsymbol{n}}, \vec{\boldsymbol{t}}, \vec{\boldsymbol{v}}$ are the unit vectors representing the direction of the light source, the surface normal, the reflected light, and the viewing point, respectively, as shown in Figure 2.1. In diffuse or Lambertian reflection, represented by the second term in Equation (2.1), the incident light is scattered equally in all directions as shown in Figure 2.2. However, the intensity of the reflected light is proportional to the cosine of the angle between the incident light and the surface normal. This is known as Lambert's cosine law [36]. In specular reflection, represented by the last term in Equation (2.1), light is reflected such that the angle of incidence equals the angle of reflection as shown in Figure 2.1. In this study, the ambient reflection component, which is the first term in the above sum, is minimized, in fact zeroed by an infrared filter, covering the detector window. Therefore, the reflected intensity is a combination

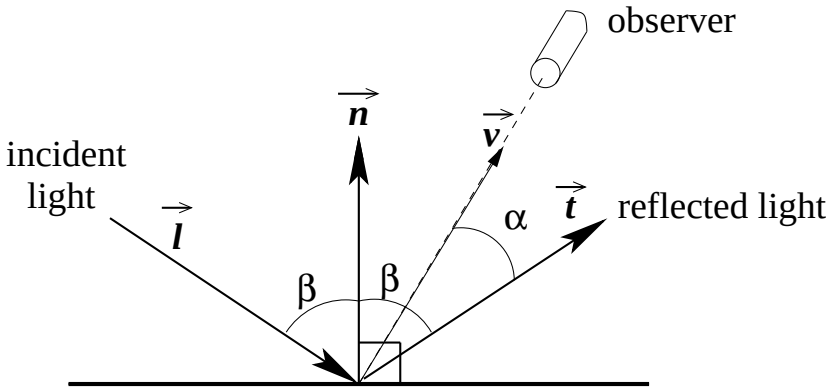

Figure 2.1: Specular reflection.

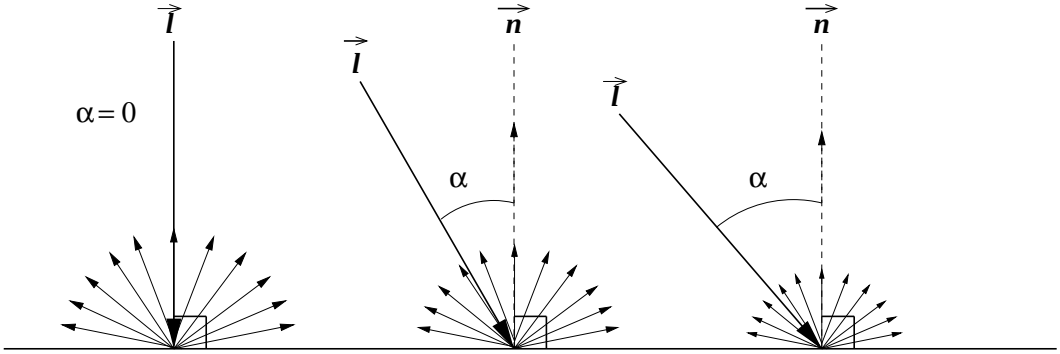

Figure 2.2: Diffuse reflection at different angles of incidence.

of diffuse and specular components.

The position of the sensors with respect to the surface is described in spherical coordinates using r (range), θ (azimuth angle), and ϕ (elevation angle) as shown in Figure 2.3. It is essential to name two critical features for clarifying the geometry of the setup depicted in Figure 2.3. The first is the *sensor plane,* on which the emitter, the detector, and their line of sights lie. The second is the *line of interest,* which is the intersection of the sensor plane with the target surface. It is the line from which the distance is measured or calculated. In our case, ϕ has a vital priority over θ as will be explained below. Therefore, determining whether ϕ equals zero or not is the first step to take.

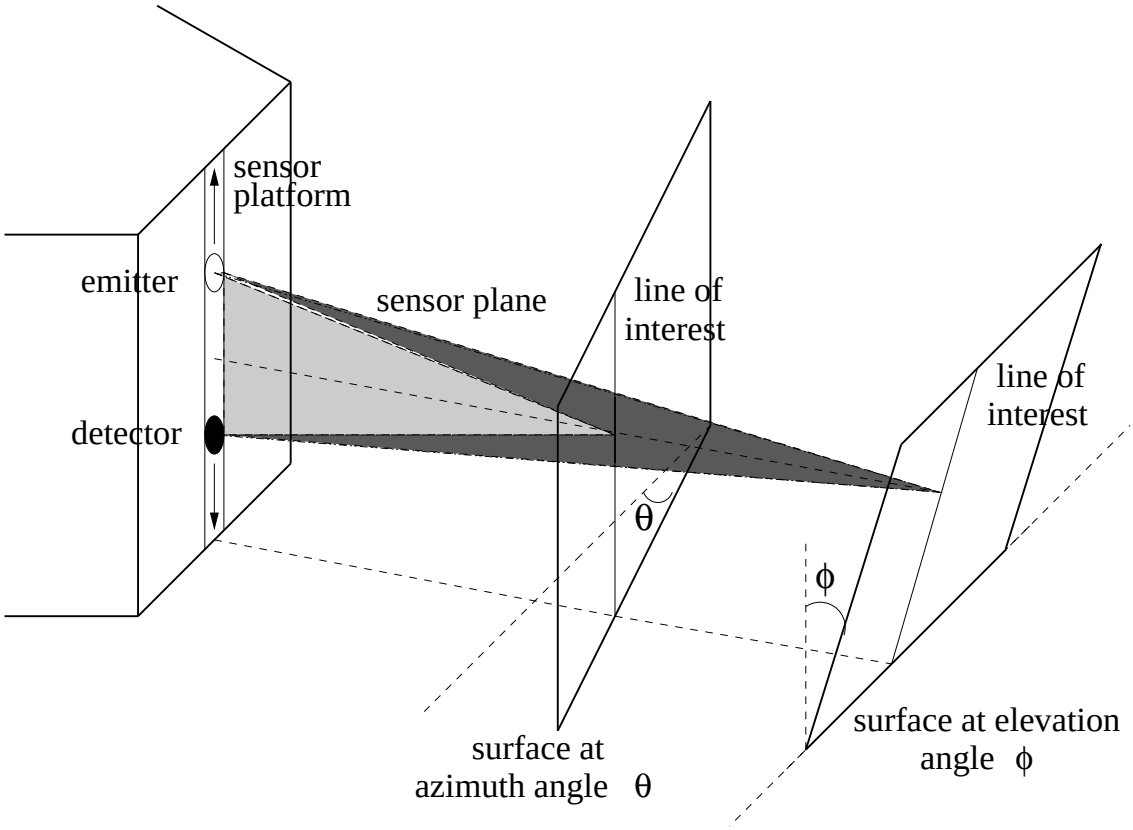

Figure 2.3: The general case where $\theta \neq 0°$ and $\phi \neq 0°$.

The cases for $\phi = 0°$ and $\phi \neq 0°$ are investigated separately in the following two subsections.

2.1 Surfaces with $\phi = 0°$

When ϕ is zero, the line of interest is parallel to the baseline of the sensors (Figure 2.4). In order for ϕ to equal zero, the following two conditions should be satisfied:

- All maximum intensity data for different positions of the emitter should be equal to each other within some given error tolerance since the sensor platform and the line of interest are parallel.
- Measured baseline separations corresponding to the maximum intensity data should be equal to each other again within some given error tolerance.

Once it is detected that $\phi = 0°$, the next step is to determine θ. In fact, the value of θ is not needed for range estimation. To show this, let us first consider the simple case where both ϕ and θ are equal to zero.

2.1.1 $\phi = 0°, \theta = 0°$

When ϕ and θ are both equal to zero, both specular and diffuse reflection components are effective. Due to specular reflection properties, the detector senses the maximum specular reflection component at position 1 where $\psi_i = \psi_r = \psi$ as shown in Figure 2.5. Although diffusely reflected light is scattered equally in all directions as shown in the figure, the detector senses the diffuse reflection component maximally again at position 1 where there is a component of the reflection in alignment with the detector line of sight, as shown in Figure 2.5. Therefore, diffuse and specular reflection components act the same way to maximize the detector reading when the emitter and the detector are equidistant from the surface

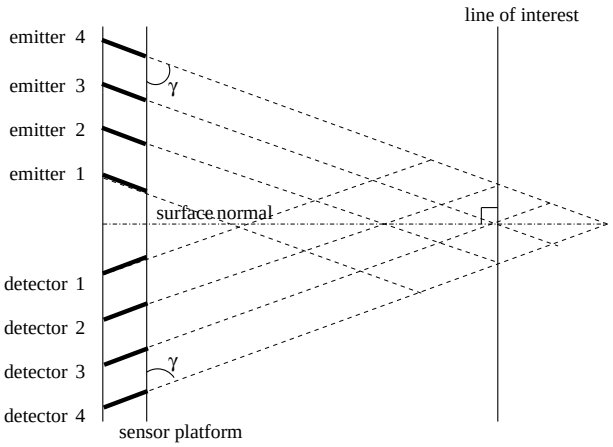

Figure 2.4: Cross-section of the experimental setup when the line of interest is parallel to the baseline of the sensors ($\phi = 0°$).

normal. The distance between the sensor platform and the line of interest can be easily calculated as:

$$r = a \tan \gamma \tag{2.2}$$

where a is the half of the baseline separation between the emitter and the detector when the detector senses the maximum intensity data and γ is the angle made between the sensor line of sight and the linear platform.

2.1.2 $\phi = 0°, \theta \neq 0°$

When ϕ is zero but θ is not, specular reflection has no effect on the detector reading since the line of sight of the detector does not lie on the plane where the specularly reflected beam propagates, as shown in Figure 2.6. Thus, the detector reading is completely dominated by the diffuse reflection component, as shown in Figure 2.7. However, only the reflected beam which propagates on the sensor plane is effective whereas the others propagating on the other planes are not sensed. Therefore, the situation simplifies to the representation of diffuse reflection in Figure 2.5. The detector output is again maximum at position 1 where the detector line of sight intersects the point of reflection so that there is

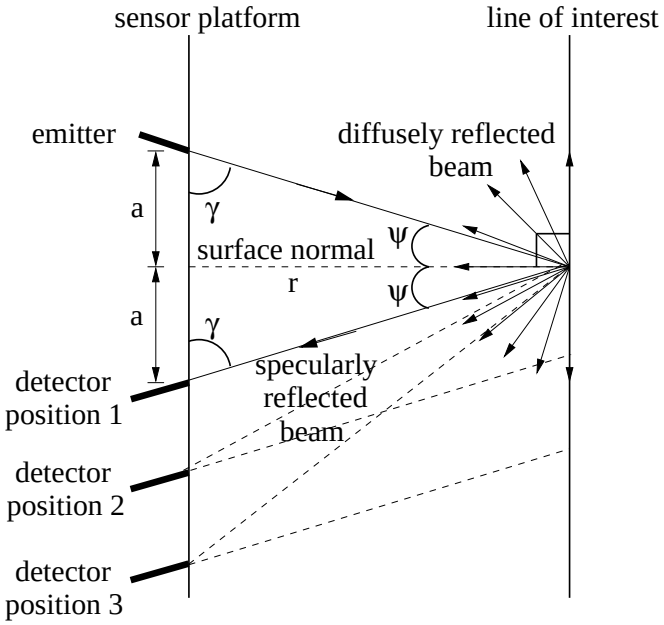

Figure 2.5: Sensing the specularly and diffusely reflected components.

a component of the diffusely reflected beam which is in alignment with the line of sight of the detector. Hence, the distance between the linear platform and the line of interest is calculated similar to the first case, using Equation (2.2).

2.2 Surfaces with $\phi \neq 0°$

When $\phi \neq 0°$, the procedure to follow is more complex as the line of interest is not parallel to the baseline of the sensors anymore. This means that the distance between the line of interest and the baseline is variable. It should also be noted that similar to the $\phi = 0°$ case, the value of θ does not affect the way the range is estimated. Therefore, for this case, θ is set to zero, in order not to increase the complexity of the geometry of the experimental setup.

The cross-section of the setup is given in Figure 2.8. From the very small values of ϕ (starting at about 3°), specular reflection becomes non-detectable by the detector since, depending on the range, the specularly reflected infrared beam either reaches the detector with a large angle which remains outside the cone-like

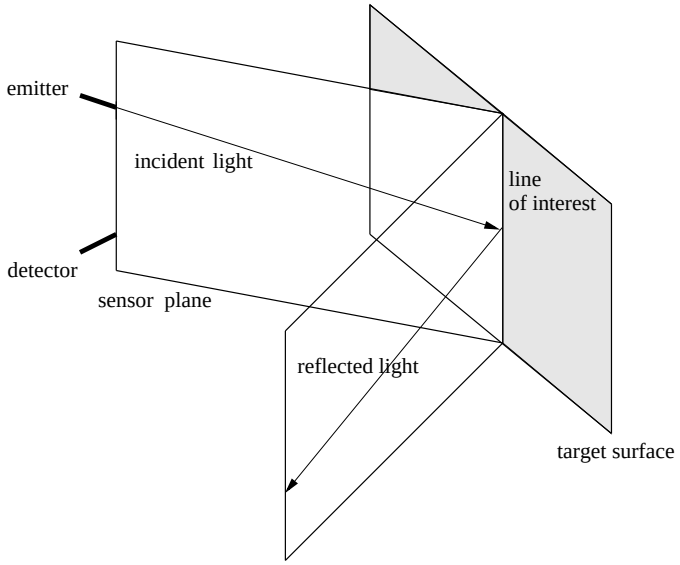

Figure 2.6: Specularly reflected light propagating on a distinct plane when $\theta \neq 0°$.

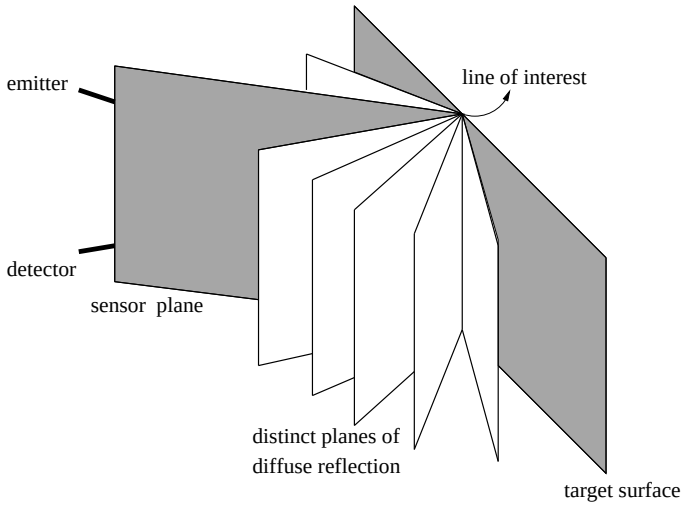

Figure 2.7: Diffusely reflected light propagating on distinct planes.

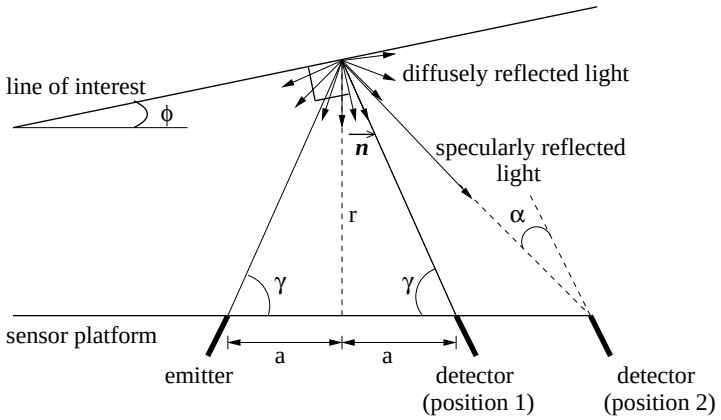

Figure 2.8: The cross-section of the experimental setup.

beam pattern or is spread out of the limits of the sensor platform. As this study is realized with 5° increments in ϕ, the effects of specular reflection for small ϕ values ($\phi \leq 3°$) are not considered. Therefore, what the detector senses is only the diffuse reflection component.

If infrared sensors are regarded as point sources (infrared beam approximated as a single ray), then the distance from the baseline of the sensors (from the midpoint of emitter-detector separation) to the line of interest can be calculated as in the $\phi = 0°$ case. However, this approach has resulted in erroneous range estimates for the $\phi \neq 0°$ case. The error in the estimates can be explained as follows: In the case where $\phi = 0°$, among all the rays within the cone-like beam-pattern, the ray corresponding to the line of sight of the sensor travels the shortest distance and reaches the surface first, causing the most powerful reflection. The path this ray travels corresponds to the range we want to estimate, causing no problems. However, when $\phi \neq 0°$, the ray experiencing the shortest distance of travel is no longer the one corresponding to the line of sight of the sensor. The region, where the most powerful reflection occurs is now shifted to the left of the line of sight. Thus, we need to improve the model, as in Figure 2.9, where β is the additional angle from the line of sight of the emitter to the point where the most powerful reflection occurs, r is the actual distance we want to estimate, corresponding to the distance from the midpoint of the emitter/detector pair to the surface and ρ

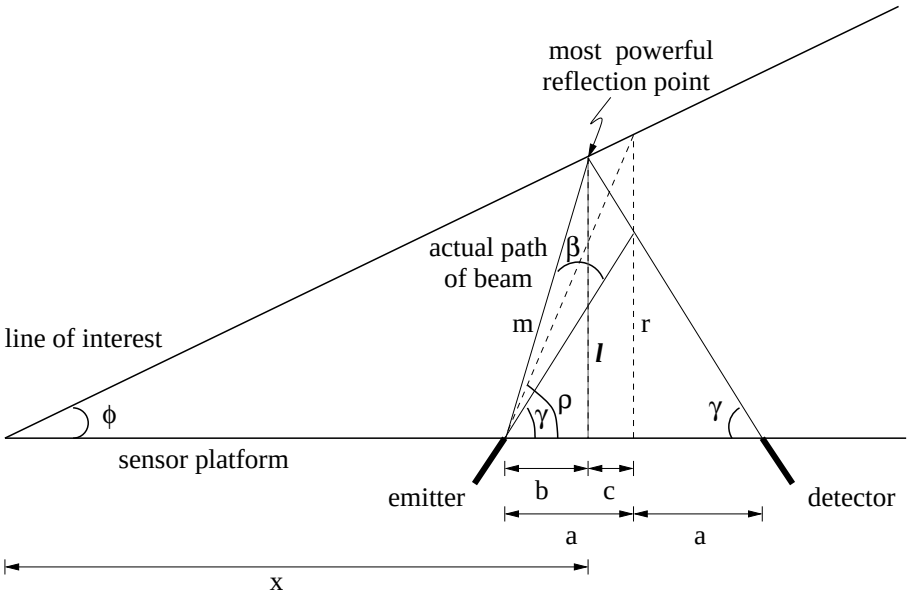

Figure 2.9: The improved model of the experimental setup.

is the angle between the linear platform and the line connecting the emitter and the intersection point of r line with the line of interest. Hence, apart from ϕ, β should be determined to obtain l, which is the distance from the most powerful reflection point to the baseline of the sensors. It should be noted that the point where the line of length l intersects the baseline of the sensors is not the mid-point of emitter-detector separation, which makes the calculations more complex. As β is fixed for a specific value of ϕ, if it can be shown that ρ is also fixed, then r can be used instead of l. The details of the proof showing that ρ is fixed under constant ϕ and β are provided in Appendix A.

The fact that ρ depends only on ϕ and β, enables us to use ρ and r instead of l for range estimation. This is extremely advantageous since the line of length r intersects the baseline at the mid-point of the emitter-detector separation, whereas the position where the line of length l intersects the baseline needs computing. The ρ values are experimentally found and recorded for different ϕ values as explained later in Section 3. These data will be used to find ρ values for an arbitrary value of ϕ using linear interpolation.

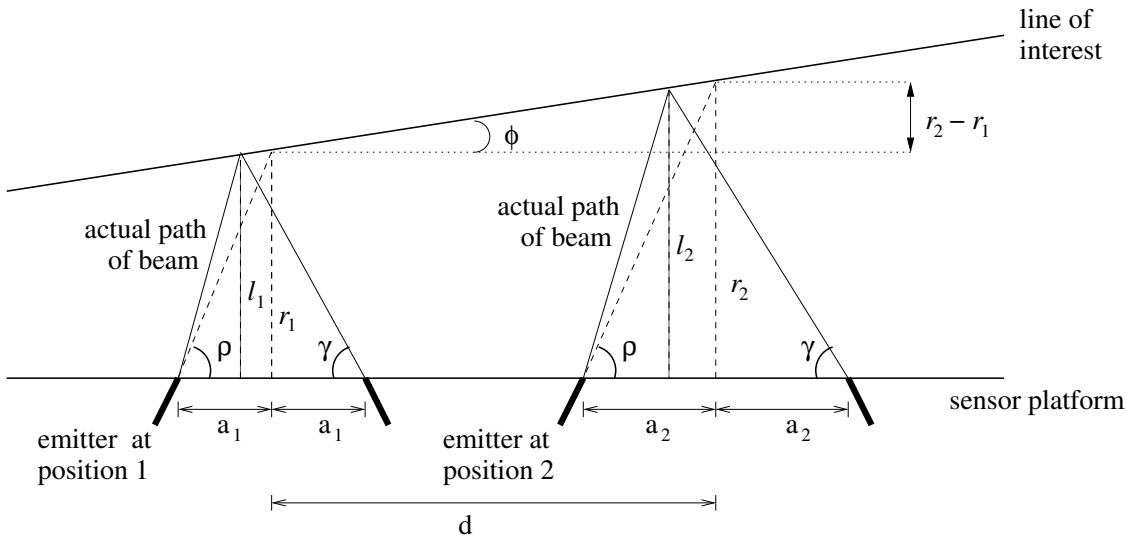

Figure 2.10: Range estimation when $\phi \neq 0°$.

As ρ depends on ϕ, the value of ϕ for any configuration should be determined. The procedure we followed is as follows: two distinct positions of the emitter are chosen and the corresponding detector locations where maximum intensity data are sensed are found as shown in Figure 2.10. The distances between the emitter and the detector are recorded as $2a_1$ and $2a_2$, and the distance between the mid-point of the first baseline separation and the mid-point of the second baseline separation is denoted as d. As shown in the figure:

$$\begin{aligned} r_1 &= a_1 \tan\rho \\ r_2 &= a_2 \tan\rho \\ \tan\phi &= \frac{r_2 - r_1}{d} = \frac{a_2 - a_1}{d} \tan\rho \end{aligned}$$

Hence, $\tan\rho$ can be calculated as follows:

$$\tan\rho = \tan\phi \, \frac{d}{a_2 - a_1} \tag{2.3}$$

Since ρ is constant for a given ϕ, it is reliable to use $(a_2 - a_1)/d$ as an indicator of ϕ. To do that, $(a_2 - a_1)/d$ data for specific ϕ are experimentally obtained. The data acquired experimentally are recorded in order to estimate the corresponding $\tan\phi$ value by linear interpolation.

The whole procedure to find the distance between the line of interest and the baseline of the sensors can be summarized as follows:

- If ϕ is not zero, $(a_2 - a_1)/d$ ratio is found and the corresponding ϕ value is extracted using linear interpolation on the $(a_2 - a_1)/d$ versus ϕ curve.
- Once ϕ is known, $\tan\rho$ can be found by interpolating on the $\tan\rho$ versus ϕ curve.
- Once $\tan\rho$ is known, the distance from the mid-point of emitter-detector separation to the line of interest is found using either of the following equations:

$$\begin{aligned} r_1 &= a_1 \tan\rho \\ r_2 &= a_2 \tan\rho \end{aligned} \tag{2.4}$$

where r_1 is the distance from the midpoint of emitter/detector pair to the line of interest for the first position of emitter and r_2 is the same for the second position of the emitter.

Chapter 3

EXPERIMENTAL VERIFICATION

3.1 Experimental Setup

The experimental setup (Figure 1.2) is composed of a vertical linear platform, two stepper motors, two infrared sensors and a 10-bit A/D converter chip, all of which are controlled by a single PC with two parallel ports. The setup also includes interface circuits where needed. The data sheets of the above mentioned components of the system are given in Appendix B.

Both of the infrared sensors [37] used in this study include an emitter and a detector in a metal casing (Figure 1.1). However, to use the sensors as a separate emitter-detector pair, the detector of one of the sensors and the emitter of the other are inhibited by covering them with an appropriately sized opaque material. The emitter and the detector both make a pre-determined angle ($\gamma = 60^{\circ}$) with the platform on which they slide, as shown in Figure 2.4.

The sensors work with 20–28 V dc input voltage and provide analog output voltage proportional to the measured intensity reflected off the target. The window of the operational detector has been covered with an infrared filter by the

manufacturer to minimize the effect of ambient light on the intensity measurements. Indeed, when the emitter is turned off, the detector reading is essentially zero. The sensitivity of the device can be adjusted with a potentiometer to set the operating range of the system. The detector output is interfaced to the PC after it is processed by a 10-bit microprocessor-compatible A/D converter chip having a conversion time of 100 μsec and 10 mV resolution. Initially, we used an 8-bit A/D converter chip which did not provide sufficient accuracy. With the present configuration, the detector output ranges between 0 to 4.9 V, where saturation occurs at 4.9 V.

The linear platform constitutes the basis for the linear motion of the detector with the help of a 5.1 W stepper motor. The stepper motor is connected to a 70 cm long infinite screw made of steel on which the detector moves up and down over a 60 cm range. The platform also possesses two support rods made of steel on both sides of the infinite screw as shown in Figure 1.2. A stepper motor is directly connected to the upper end of the infinite screw so that the rotation of the stepper motor is converted to a linear motion in the vertical direction. The step size of the motor is 1.8° corresponding to 0.04 cm linear displacement of the detector at each step. To be able to record the distance between the emitter and the detector, it is sufficient to keep track of the number of steps the motor takes. Counter-clockwise rotation of the stepper motor moves the detector upward and a clockwise rotation results in downward motion.

The second stepper motor is directly connected to the potentiometer of the detector to set the sensitivity of the device automatically. In fact, it is used to decrease the sensitivity of the detector when the acquired intensity data is saturated as explained in more detail in Section 3.2.

The whole system is 90 cm high and weighs around 10 kg including the sensors and the stepper motors. The overall cost of such a system is around 300 USD including the motors but not the sensors and the PC. The system provides high precision in linear motion together with high stability.

3.2 Experimental Results

First, we wanted to check the repeatability of the experimental data acquired and see if there is significant difference between data acquired during upward and downward motion. For this purpose, for a fixed position of the emitter, the detector slides upward along the sensor platform to record the intensity data and the corresponding baseline separation at each step of the stepper motor. Once the upward motion is completed, the detector changes direction and slides downward at the same sensitivity setting. In Figures 3.1 and 3.2, the data acquired during the upward and downward motion is shown for two different types of surfaces and it is seen that they are very close to each other except for some slight differences. Since there is not a significant difference between data collected during upward and downward motion, we conclude that the data are repeatable.

In the next step, to quantify the noise fluctuations and the uncertainty of the intensity data, we collected 100 intensity data at each step of the motor and recorded the mean and the standard deviation of these data, together with the corresponding baseline separation. The results are shown in Figures 3.3 and 3.4 for the same two surfaces where the mean intensity data are plotted together with plus/minus ten standard deviations. In Table 3.1, standard deviation values at the maximum intensity position of the intensity curve and the maximum standard deviation value of the complete curve are tabulated at four different distances. The standard deviation values do not seem to have a dependence on distance. The values for wood are, in general, larger than those obtained for white paper. Since the maximum intensity that can be measured by the system corresponds to 4.9 V, it can be concluded that the standard deviation is at most 1% of the saturation intensity.

The procedure followed for range estimation is as follows: For a given fixed position of the emitter, the detector starts to slide upward along the sensor platform to collect and record intensity data and the corresponding baseline separation at each step of the stepper motor. During its motion, the detector collects 100 intensity data at each step of the stepper motor and the mean of these data is recorded together with the corresponding baseline separation. As soon as the

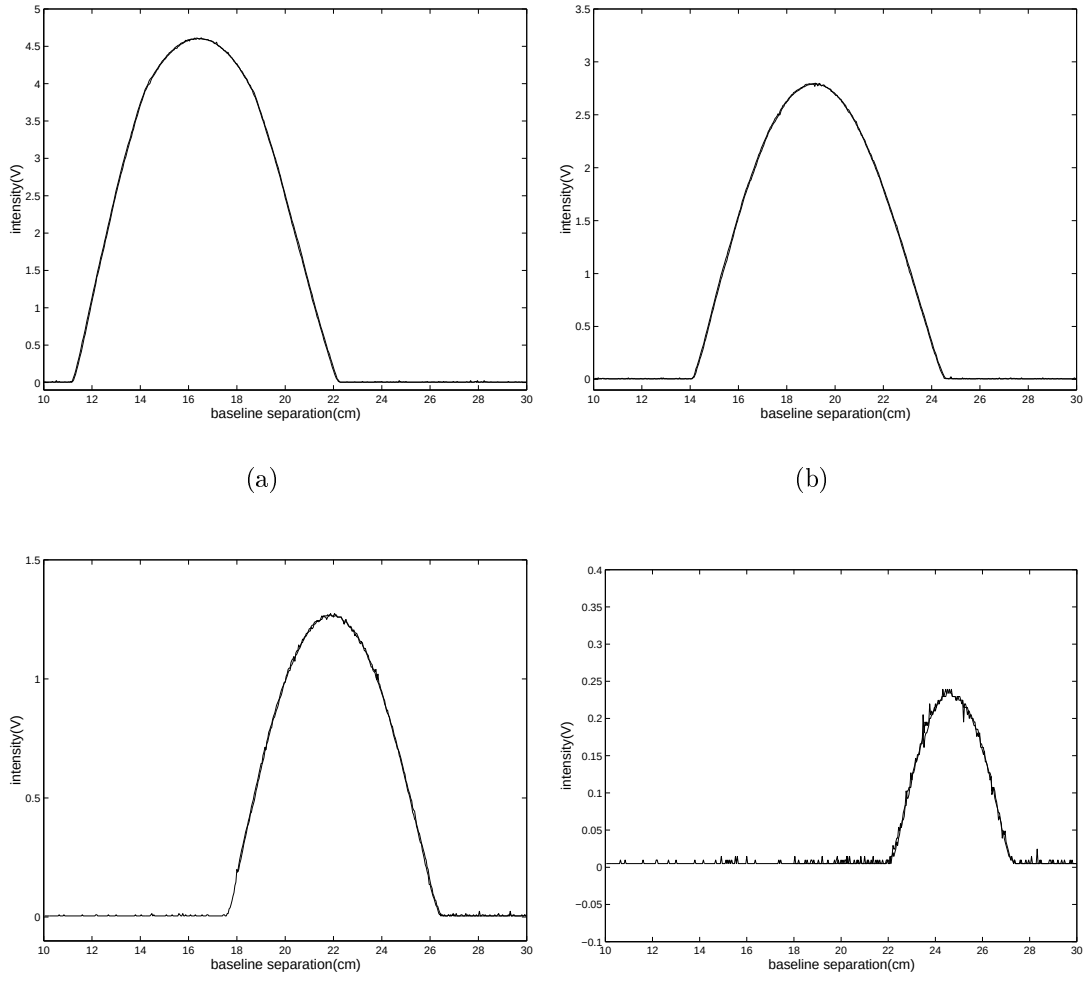

Figure 3.1: Data acquired during upward and downward motion for a wooden planar surface at (a) 15 cm, (b) 17.5 cm, (c) 20 cm, (d) 22.5 cm.

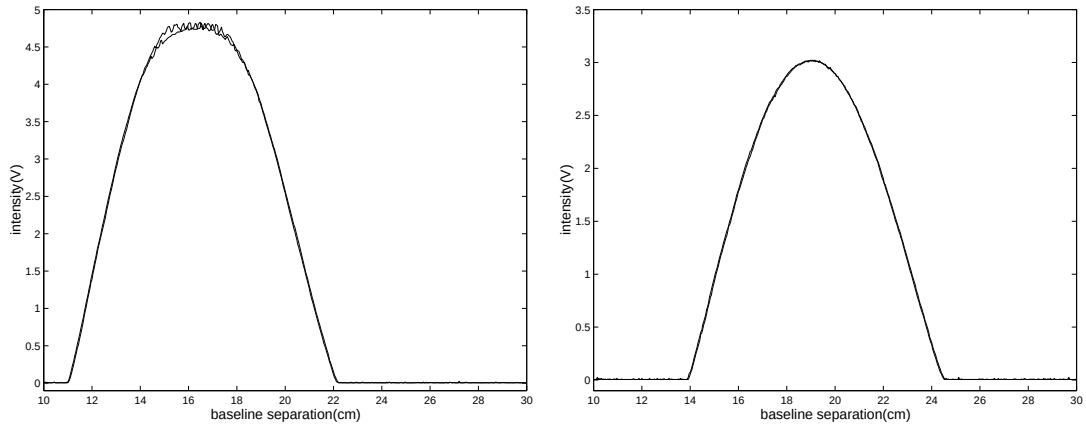

(a) (b)

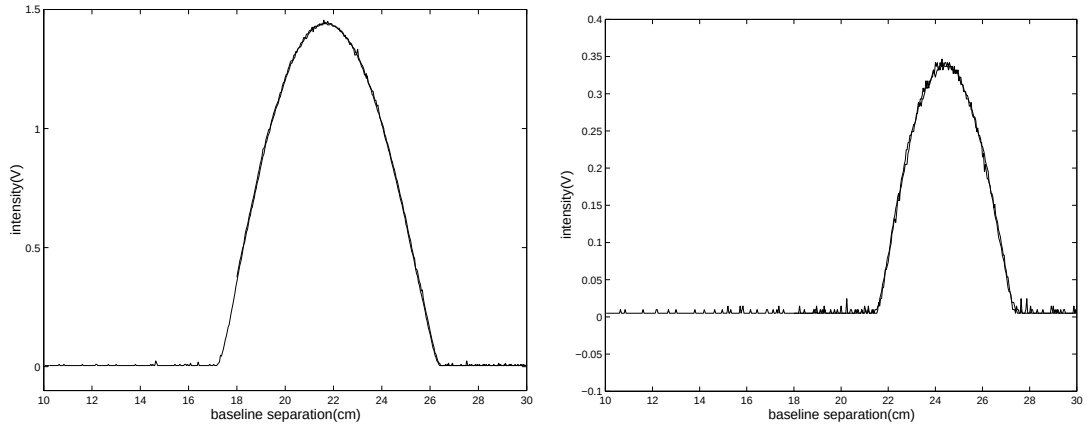

(c) (d)

Figure 3.2: Data acquired during upward and downward motion for a planar surface covered with white paper at (a) 15 cm, (b) 17.5 cm, (c) 20 cm, (d) 22.5 cm.

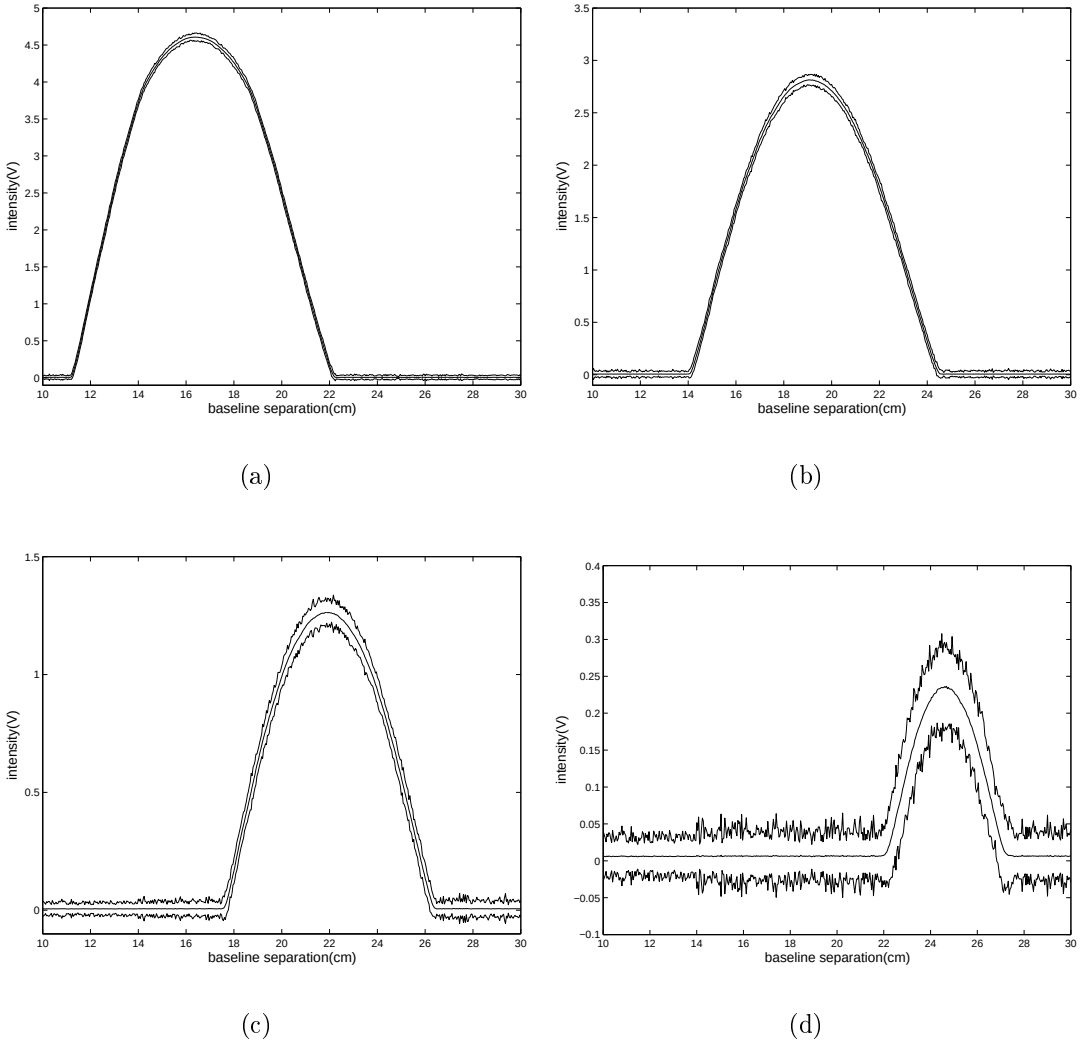

Figure 3.3: The mean intensity plus/minus ten standard deviations for a wooden planar surface at (a) 15 cm, (b) 17.5 cm, (c) 20 cm, (d) 22.5 cm.

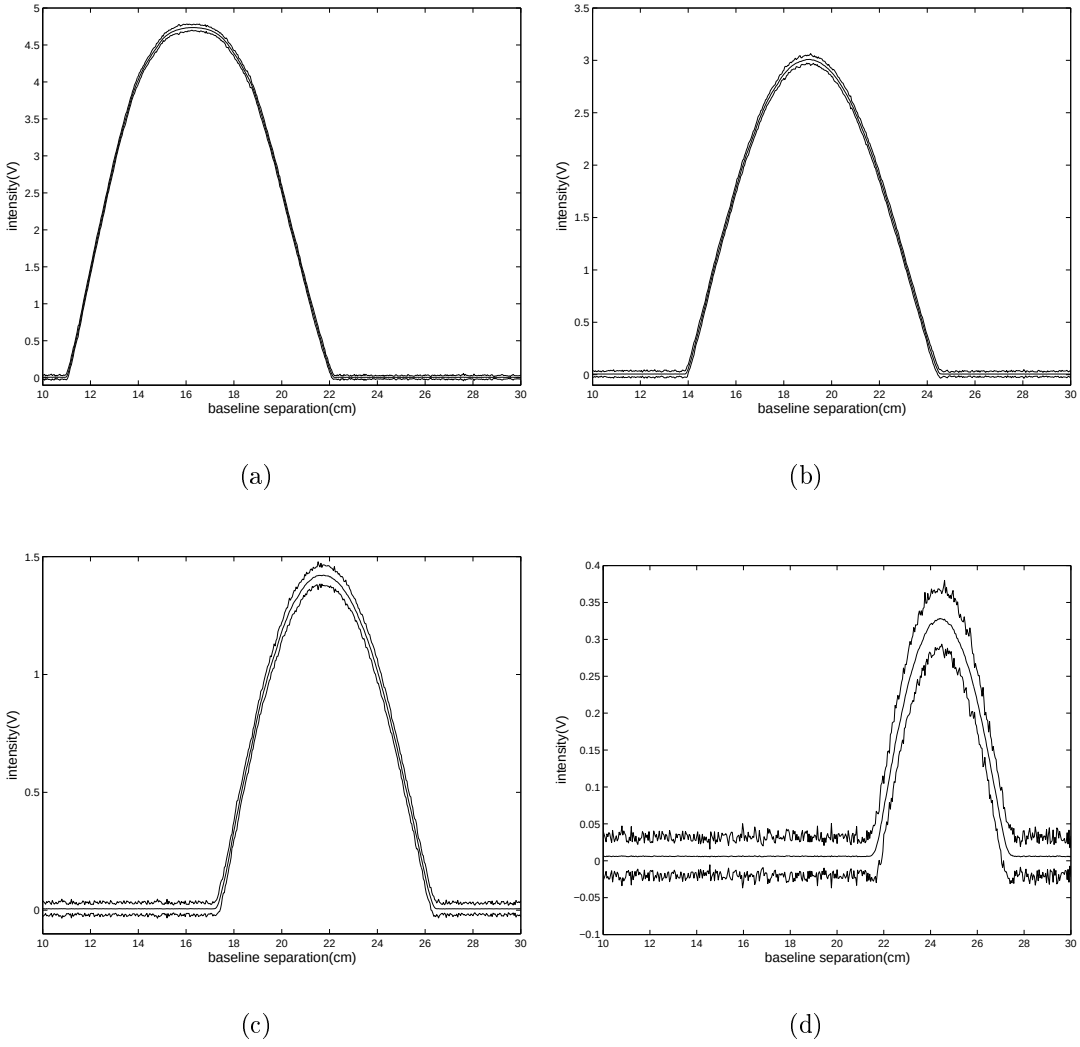

Figure 3.4: The mean intensity plus/minus ten standard deviations for a planar surface covered with white paper at (a) 15 cm, (b) 17.5 cm, (c) 20 cm, (d) 22.5 cm.

Table 3.1: Standard deviation values for wood and white paper at different ranges.

	std(V) at max intensity		max std(V)	
r(cm)	wood	white paper	wood	white paper
15.0	0.0046	0.0045	0.0079	0.0078
17.5	0.0052	0.0044	0.0094	0.0057
20.0	0.0053	0.0034	0.0081	0.0063
22.5	0.0059	0.0033	0.0088	0.0055

upward motion ends, the intensity data is checked for saturation. An intelligent feature of our experimental setup is the automatic adjustment of the sensitivity of the detector. Four different sensitivity settings are available. Initially, the detector is set to the maximum sensitivity setting. If saturation is detected during the upward motion, the second stepper motor adjusts the sensitivity of the detector to a lower setting. Based on the center of gravity of the saturated intensity data obtained during the upward motion, it is possible to make a rough estimate of the distance to the surface. Using this estimate, the sensitivity of the detector can be adjusted usually in one step and this adjusted setting is used throughout the downward motion.

When the detector returns to its initial position after the downward motion, the data acquired is inspected for saturation. If saturation still exists, the sensitivity is further decreased and another set of data is acquired. In very few cases where the surface is very close to the sensors, saturation still exists even with the lowest sensitivity setting. In those cases, the data is processed in the same way as the data without saturation. In the following experiments, data acquired during the last (first or second) downward motion (where saturation is eliminated whenever possible) is employed.

As soon as the detector completes its motion, the intensity data are inspected to find the maximum intensity data and the corresponding baseline separation.

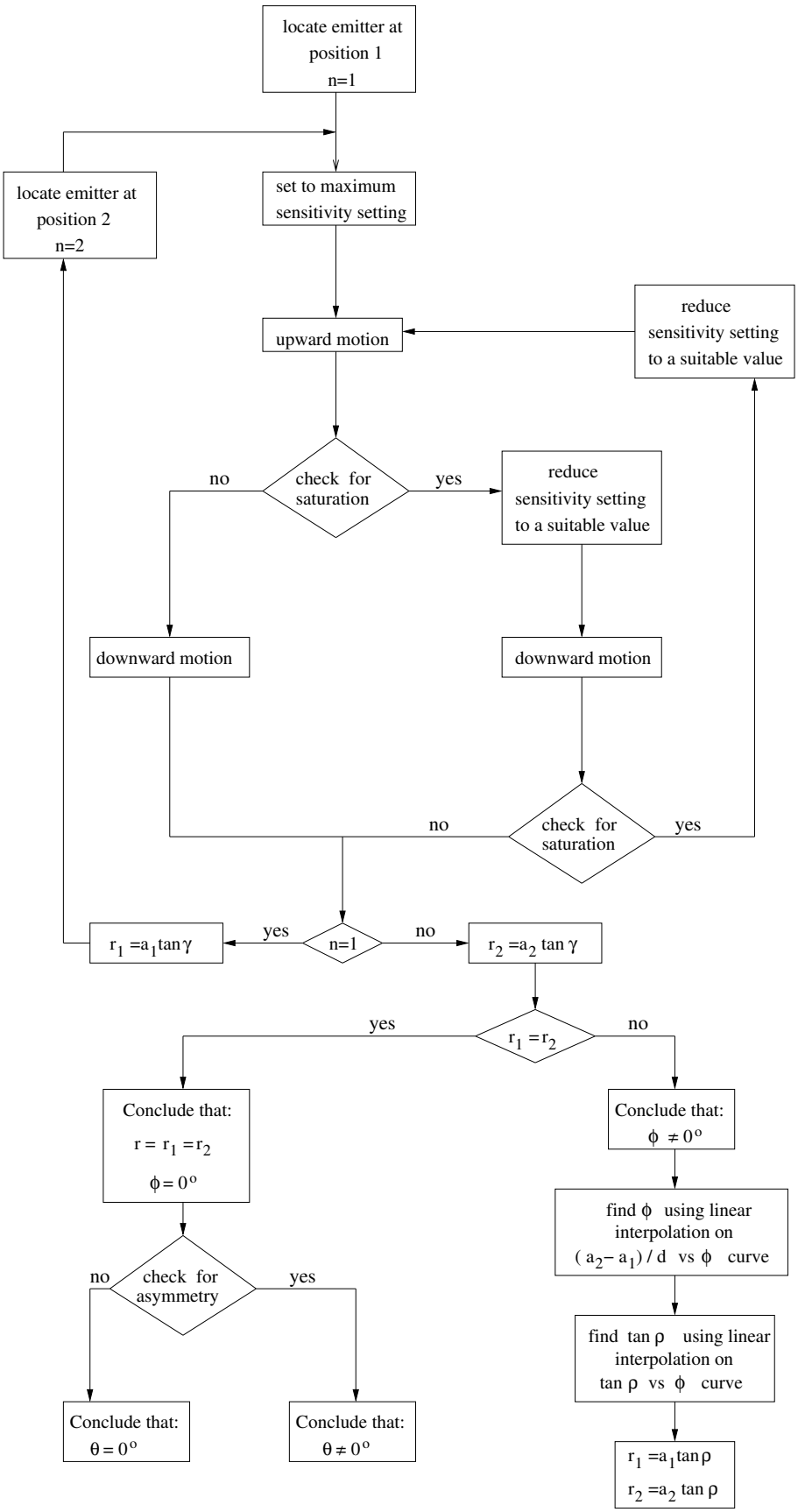

Figure 3.5: Flowchart of the procedure followed.

These are recorded for the current position of the emitter. Flowchart of the procedure followed is given in Figure 3.5. The procedure is repeated for a second position of the emitter, resulting in another set of position-intensity data. As shown in Figure 2.4, when the emitter is at position 4, detector sensing is maximum when the detector is at position 2 and similarly when the emitter is at position 3, maximum reading is acquired when the detector is at position 3, and so on.

The proposed method is verified experimentally. A planar surface of dimension 0.5m×1m×1cm is used which is made of solid wood. The surface is either left as plain wood or covered with white paper, bubbled packing material, white Styrofoam, blue, black, and red cardboard. The results are discussed in the following subsections.

3.2.1 Experimental results when $\phi = 0°, \theta = 0°$

Reference data sets are collected for each different surface, exhibiting different reflection properties, from 10 to 50 cm with 2.5 cm distance increments. As explained in Section 2.1.1, for this case, it is sufficient to find the value of a, which is half of the baseline separation between the emitter and the detector when the detector senses the maximum intensity data. To find the value of a, we used three different ways of processing the acquired intensity scan-signals based on using the positions corresponding to the i)maximum intensity value, ii)midpoint after thresholding, and iii)center of gravity (COG) of the intensity curve.

In the first method, the intensity data is searched for a single maximum. If a single maximum exists, the corresponding baseline separation ($2a$) is recorded. However, in many instances, there may be multiple maximum intensity data. That is, the detector senses maximum intensity data at a number of positions which are not necessarily consecutive. Therefore, these data should be processed to find a single position value. If multiple maxima exist, then the mean of the corresponding baseline separations are found.

In the second method, the intensity data is thresholded to retain as many samples as possible from the body of the intensity curve. The mid-point of the intensity values remaining above the threshold is found and the corresponding baseline separation is recorded.

In the last approach, for each intensity curve, we use the same threshold value as in the second method to find the COG of the intensity values remaining above the threshold. The COG is calculated according to the formula:

$$I_{COG} = \frac{\sum_{k \epsilon I_k \geq \tau} I_k . a_k}{\sum_{k \epsilon I_k \geq \tau} a_k}$$

where I_k represents the intensity data sample, a_k represents half of the corresponding baseline separation, and τ is the threshold. Then, the baseline separation corresponding to I_{COG} is recorded.

The experimental results are given in Figures 3.6 and 3.7 and in Tables 3.2–3.5. The overall absolute mean range error using all three approaches is calculated as 0.21 cm for eight different surfaces in the range from 10 to 50 cm. The errors do not seem to show any trend with increasing range. When the three approaches are compared, it is seen that using the COG method gives the best results with an average error of 0.15 cm. The thresholding method results in 0.18 cm error and the maximum intensity method gives 0.30 cm error, which is less accurate than the other two. In the last case, the errors seem to fluctuate more compared to the other two methods. Therefore, it can be concluded that by using more samples from the body of the intensity signals, we increase the robustness of distance estimation.

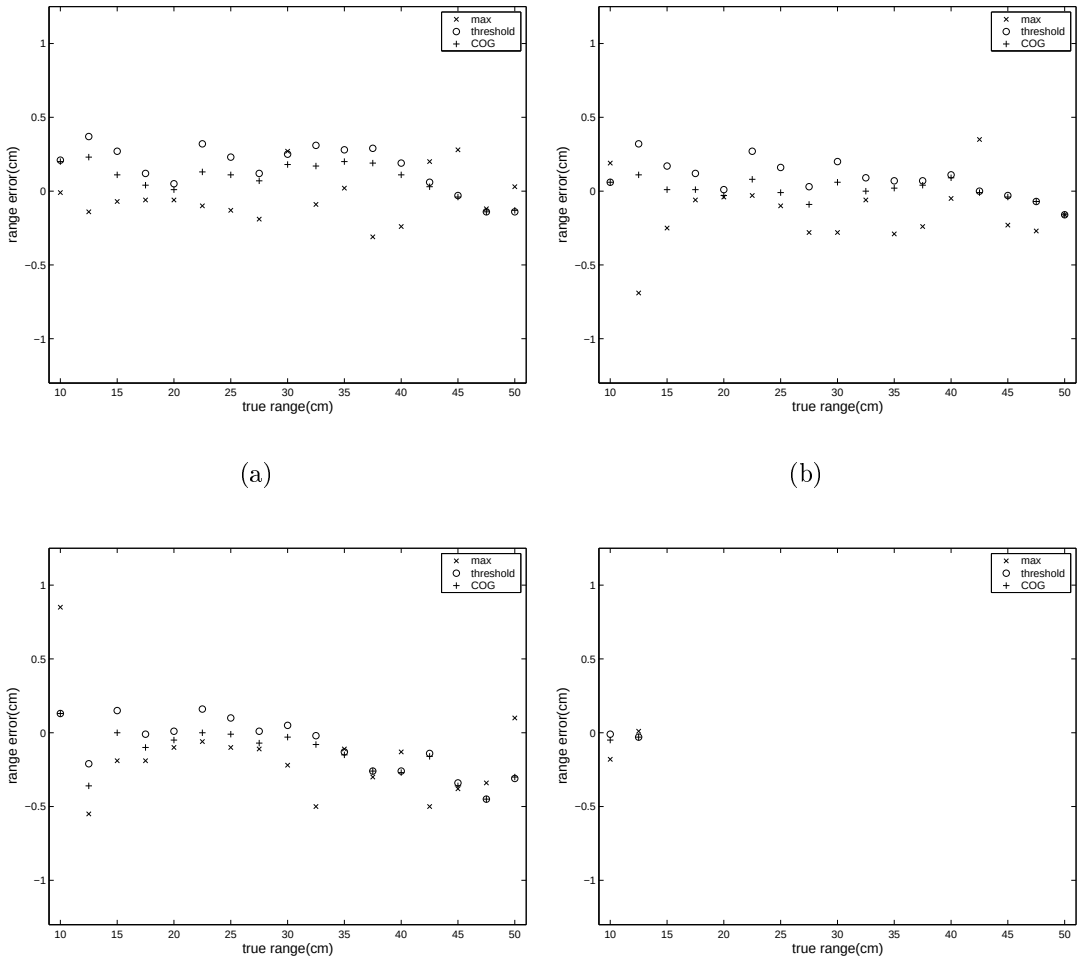

Figure 3.6: Mean range errors for different materials: (a) wood, (b) white Styrofoam, (c) white paper, (d) black cardboard.

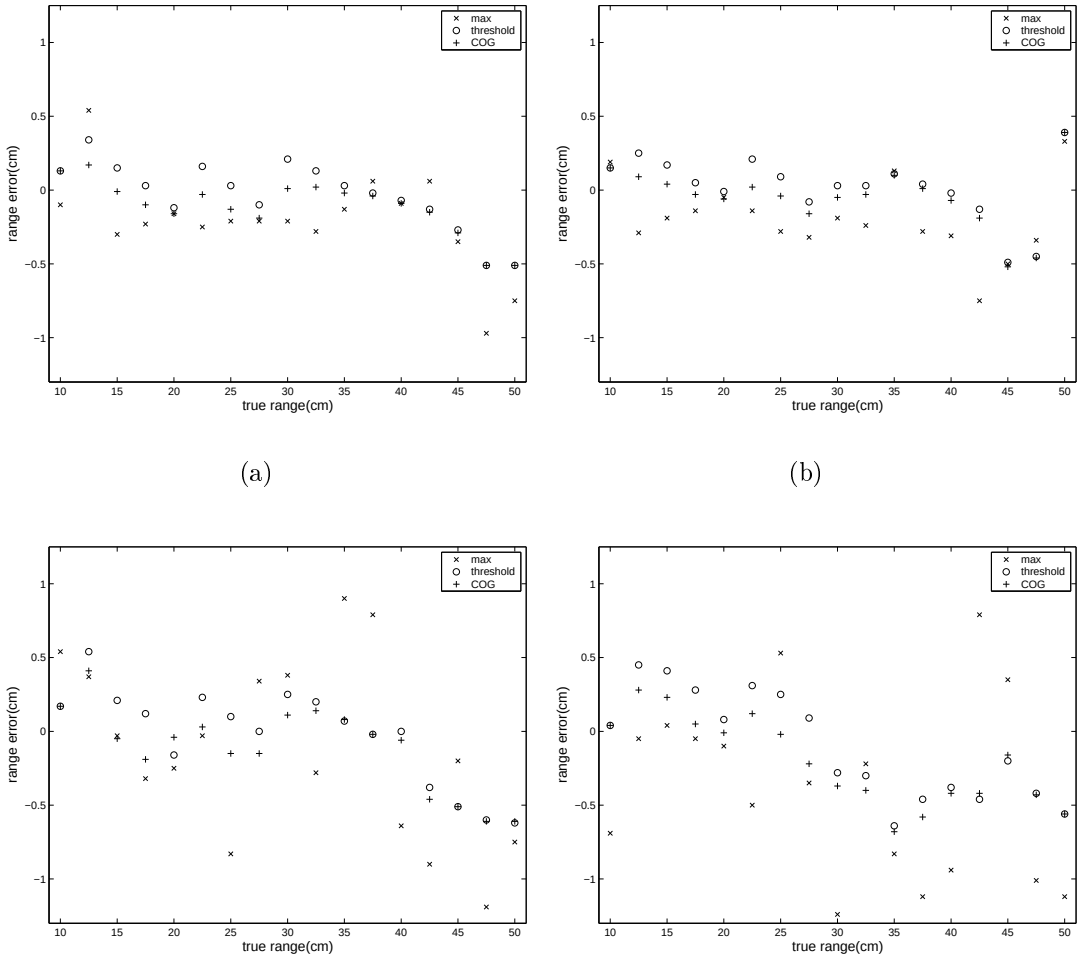

Figure 3.7: Mean range errors for different materials: (a) blue cardboard, (b) red cardboard, (c) large bubbled packing material, (d) small bubbled packing material.

Table 3.2: Range errors for wood and white Styrofoam when $\phi = 0°$ and $\theta = 0°$.

	range errors(cm)					
	wood			white Styrofoam		
true r(cm)	max	thld	COG	max	thld	COG
10.0	–0.01	0.21	0.20	0.19	0.06	0.06
12.5	–0.14	0.37	0.23	–0.69	0.32	0.11
15.0	–0.07	0.27	0.11	–0.25	0.17	0.01
17.5	–0.06	0.12	0.04	–0.06	0.12	0.01
20.0	–0.06	0.05	0.01	–0.04	0.01	–0.03
22.5	–0.10	0.32	0.13	–0.03	0.27	0.08
25.0	–0.13	0.23	0.11	–0.10	0.16	–0.01
27.5	–0.19	0.12	0.07	–0.28	0.03	–0.09
30.0	0.27	0.25	0.18	–0.28	0.20	0.06
32.5	–0.09	0.31	0.17	–0.06	0.09	0.00
35.0	0.02	0.28	0.20	–0.29	0.07	0.02
37.5	–0.31	0.29	0.19	–0.24	0.07	0.04
40.0	–0.24	0.19	0.11	–0.05	0.11	0.09
42.5	0.20	0.06	0.03	0.35	0.00	–0.01
45.0	0.28	–0.03	–0.04	–0.23	–0.03	–0.04
47.5	–0.12	–0.14	–0.14	–0.27	–0.07	–0.07
50.0	0.03	–0.14	–0.13	–0.16	–0.16	–0.16
mean error(cm)	–0.04	0.16	0.09	–0.15	0.08	0.00
absolute mean error(cm)	0.14	0.20	0.12	0.21	0.11	0.05

Table 3.3: Range errors for white paper and black cardboard when $\phi = 0°$ and $\theta = 0°$.

	range errors(cm)					
	white paper			black cardboard		
true r(cm)	max	thld	COG	max	thld	COG
10.0	0.85	0.13	0.13	–0.18	–0.01	–0.05
12.5	–0.55	–0.21	–0.36	0.01	–0.03	–0.03
15.0	–0.19	0.15	0.00			
17.5	–0.19	–0.01	–0.10			
20.0	–0.10	0.01	–0.05			
22.5	–0.06	0.16	0.00			
25.0	–0.10	0.10	–0.01			
27.5	–0.11	0.01	–0.07			
30.0	–0.22	0.05	–0.03			
32.5	–0.50	–0.02	–0.08			
35.0	–0.11	–0.13	–0.15			
37.5	–0.30	–0.26	–0.26			
40.0	–0.13	–0.26	–0.27			
42.5	–0.50	–0.14	–0.16			
45.0	–0.38	–0.34	–0.36			
47.5	–0.34	–0.45	–0.45			
50.0	0.10	–0.31	–0.30			
mean error(cm)	–0.17	–0.09	–0.15	–0.09	–0.02	–0.04
absolute mean error(cm)	0.28	0.16	0.16	0.10	0.02	0.04

Table 3.4: Range errors for blue and red cardboard when $\phi = 0°$ and $\theta = 0°$.

	range errors(cm)					
	blue cardboard			red cardboard		
true r(cm)	max	thld	COG	max	thld	COG
10.0	–0.10	0.13	0.13	0.19	0.15	0.15
12.5	0.54	0.34	0.17	–0.29	0.25	0.09
15.0	–0.30	0.15	–0.01	–0.19	0.17	0.04
17.5	–0.23	0.03	–0.10	–0.14	0.05	–0.03
20.0	–0.16	–0.12	–0.16	–0.05	–0.01	–0.06
22.5	–0.25	0.16	–0.03	–0.14	0.21	0.02
25.0	–0.21	0.03	–0.13	–0.28	0.09	–0.04
27.5	–0.21	–0.10	–0.19	–0.32	–0.08	–0.16
30.0	–0.21	0.21	0.01	–0.19	0.03	–0.05
32.5	–0.28	0.13	0.02	–0.24	0.03	–0.03
35.0	–0.13	0.03	–0.02	0.13	0.11	0.10
37.5	0.06	–0.02	–0.04	–0.28	0.04	0.01
40.0	–0.09	–0.07	–0.09	–0.31	–0.02	–0.07
42.5	0.06	–0.13	–0.15	–0.75	–0.13	–0.19
45.0	–0.35	–0.27	–0.29	–0.50	–0.49	–0.52
47.5	–0.97	–0.51	–0.51	–0.34	–0.45	–0.46
50.0	–0.75	–0.51	–0.51	0.33	0.39	0.39
mean error(cm)	–0.21	–0.03	–0.11	–0.20	0.02	–0.05
absolute mean error(cm)	0.29	0.17	0.15	0.27	0.16	0.14

Table 3.5: Range errors for large and small bubbles when $\phi = 0°$ and $\theta = 0°$.

	range errors(cm)					
	large bubbles			small bubbles		
true r(cm)	max	thld	COG	max	thld	COG
10.0	0.54	0.17	0.17	–0.69	0.04	0.04
12.5	0.37	0.54	0.41	–0.05	0.45	0.28
15.0	–0.03	0.21	–0.05	0.04	0.41	0.23
17.5	–0.32	0.12	–0.19	–0.05	0.28	0.05
20.0	–0.25	–0.16	–0.04	–0.10	0.08	–0.01
22.5	–0.03	0.23	0.03	–0.50	0.31	0.12
25.0	–0.83	0.10	–0.15	0.53	0.25	–0.02
27.5	0.34	0.00	–0.15	–0.35	0.09	–0.22
30.0	0.38	0.25	0.11	–1.24	–0.28	–0.37
32.5	–0.28	0.20	0.14	–0.22	–0.30	–0.40
35.0	0.90	0.07	0.08	–0.83	–0.64	–0.68
37.5	0.79	–0.02	–0.02	–1.12	–0.46	–0.58
40.0	–0.64	0.00	–0.06	–0.94	–0.38	–0.42
42.5	–0.90	–0.38	–0.46	0.79	–0.46	–0.42
45.0	–0.20	–0.51	–0.51	0.35	–0.20	–0.16
47.5	–1.19	–0.60	–0.61	–1.01	–0.42	–0.43
50.0	–0.75	–0.62	–0.61	–1.12	–0.56	–0.56
mean error(cm)	–0.12	–0.02	–0.11	–0.38	–0.11	–0.21
absolute mean error(cm)	0.51	0.25	0.22	0.58	0.33	0.29

3.2.2 Experimental results when $\phi = 0°, \theta \neq 0°$

Measurements are collected for the wooden surface left plain or covered with white paper from 10 to 40 cm with 10 cm distance increments at different values of θ ranging from 5° to 60° with 5° increments. In this case, the intensity curves differ from the case where $\theta = 0°$ since the curves are no longer symmetric around the peak of the curve. That is, when the slopes of the rising and the falling edges are investigated, they are observed to be significantly different. Therefore, if such an asymmetry exists, it can be concluded that $\theta \neq 0°$ as long as it is known that $\phi = 0°$. In Figure 3.8, $\theta = 0°$ and $\theta \neq 0°$ cases for the same distance are plotted together to show how these intensity curves differ.

The range estimation errors are given in Figures 3.9 and 3.10 and in Tables 3.6–3.13 with the three approaches described in the previous section. The errors start to increase for larger values of θ and also with increasing range. The reason for this increase in error can be explained by the cone-like beam pattern which causes light beams to propagate on distinct planes other than the sensor plane. The rays within the beam arrive at the surface at different times and at different angles of incidence. Since the rays experiencing shorter distance of travel or smaller incidence angle are reflected more powerfully as described by Equation (2.1), the region where the most powerful reflection occurs is shifted to the left of the line of sight. At larger values of θ, this effect is more enhanced and causes larger range errors.

When the three approaches are compared, it is seen that, for this case, the thresholding method gives the best results. However, the COG method gives comparable results to that of the thresholding method. As in the previous case, the maximum intensity method again gives the least accurate results.

In conclusion, the range is estimated in the same way regardless of whether $\theta = 0°$ or $\theta \neq 0°$. However, the value of θ affects the accuracy of range estimation since the range error increases with θ.

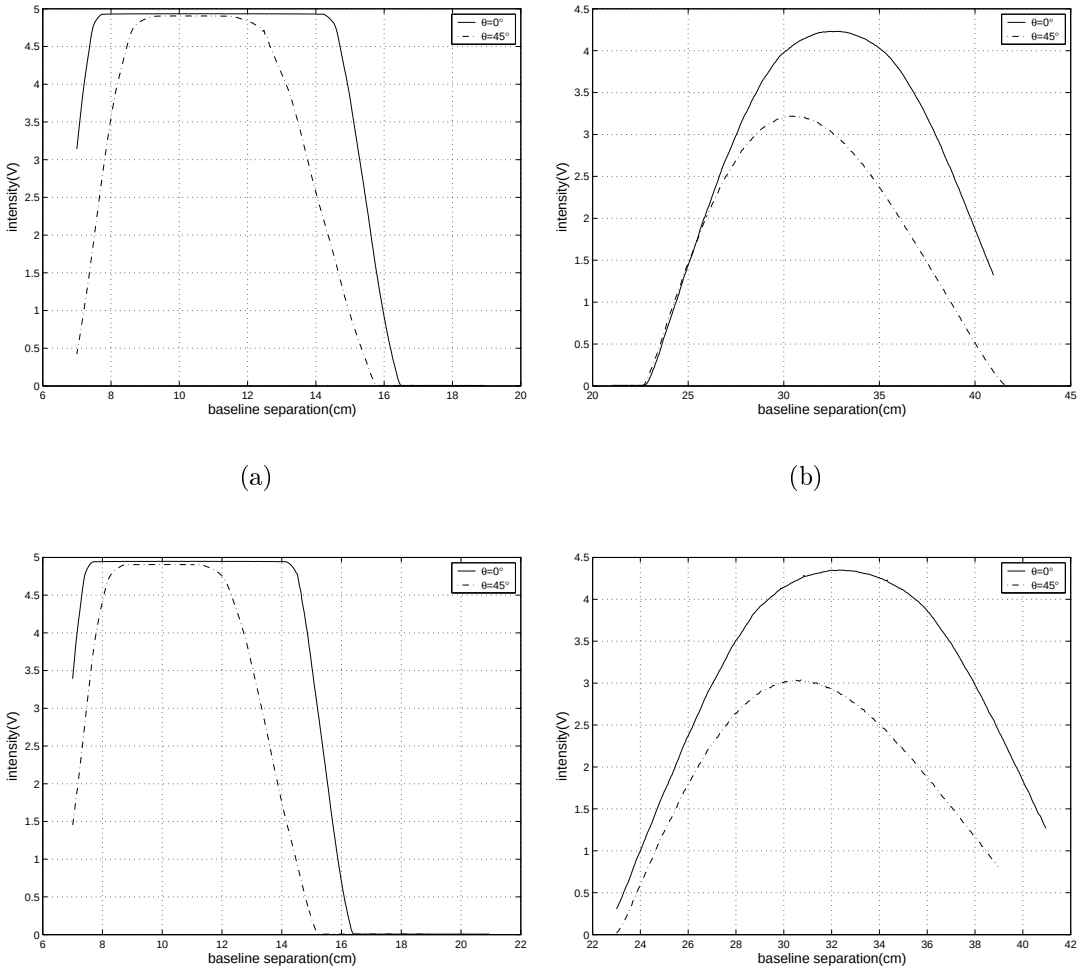

Figure 3.8: Intensity curves for $\theta = 0°$ and $\theta \neq 0°$. Wooden surface at (a) 10 cm, (b) 30 cm; surface covered with white paper at (c) 10 cm, (d) 30 cm.

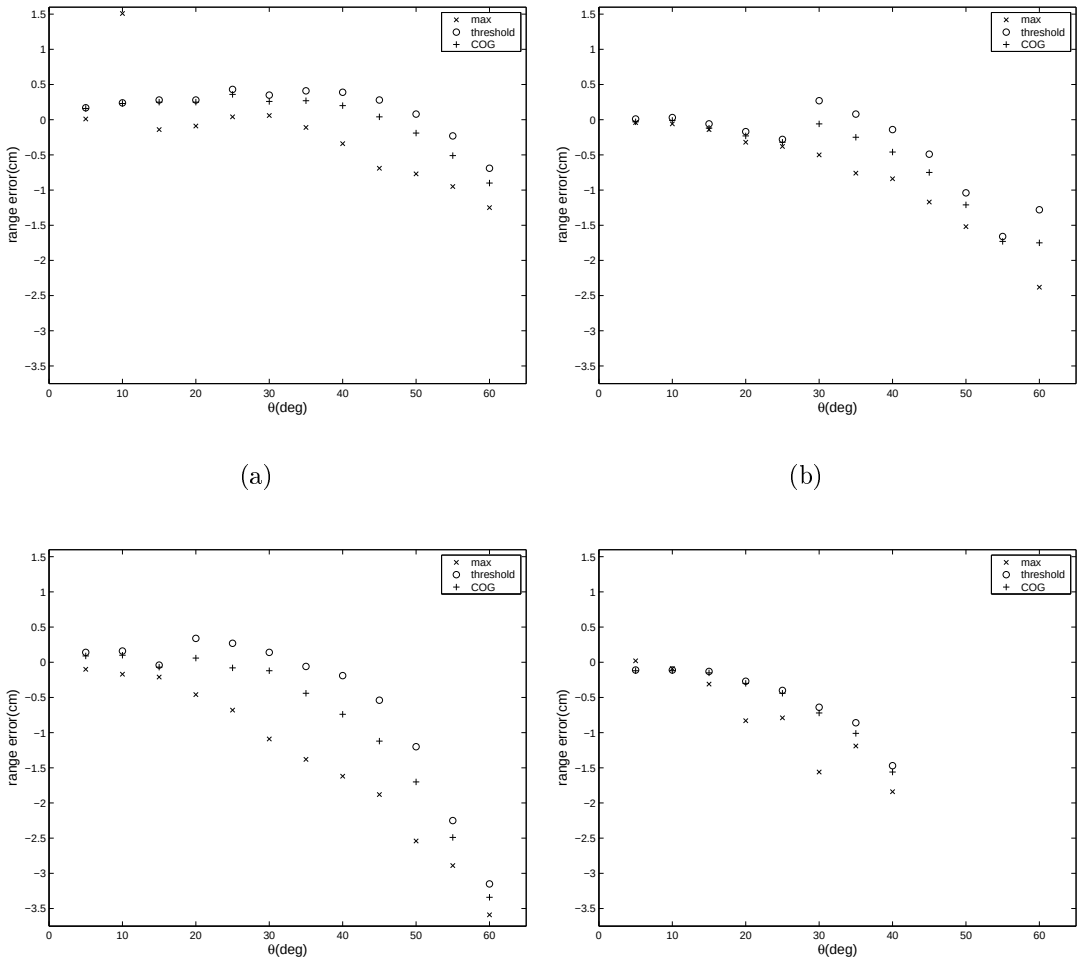

Figure 3.9: Mean range errors for different θ values for wooden surface at (a) 10 cm, (b) 20 cm, (c) 30 cm, (d) 40 cm.

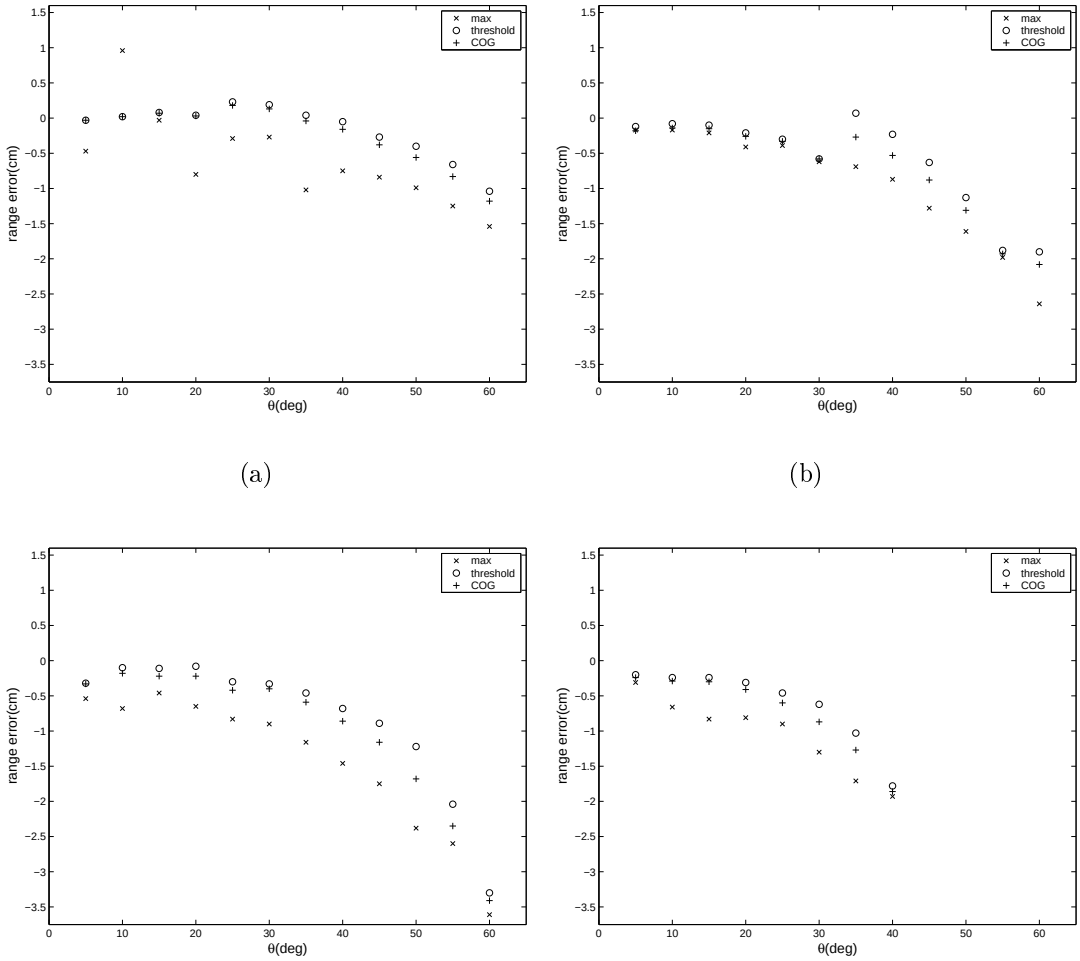

Figure 3.10: Mean range errors for different θ values for white paper at (a) 10 cm, (b) 20 cm, (c) 30 cm, (d) 40 cm.

Table 3.6: Range estimates and errors for wood at 10 cm when $\phi = 0°$ and $\theta \neq 0°$.

	r estimate(cm)			error(cm)		
θ(deg)	max	thld	COG	max	thld	COG
5.0	10.0	10.2	10.2	0.01	0.17	0.16
10.0	11.5	10.2	10.2	1.51	0.24	0.23
15.0	9.9	10.3	10.3	–0.14	0.28	0.25
20.0	9.9	10.3	10.2	–0.09	0.28	0.25
25.0	10.0	10.4	10.4	0.04	0.43	0.36
30.0	10.1	10.4	10.3	0.06	0.35	0.26
35.0	9.9	10.4	10.3	–0.11	0.41	0.27
40.0	9.7	10.4	10.2	–0.34	0.39	0.20
45.0	9.3	10.3	10.0	–0.69	0.28	0.04
50.0	9.2	10.1	9.8	–0.77	0.08	–0.19
55.0	9.0	9.8	9.5	–0.95	–0.23	–0.51
60.0	8.8	9.3	9.1	–1.25	–0.69	–0.90
mean error(cm)				–0.23	0.17	0.04
absolute mean error(cm)				0.50	0.32	0.30

Table 3.7: Range estimates and errors for wood at 20 cm when $\phi = 0°$ and $\theta \neq 0°$.

	r estimate(cm)			error(cm)		
θ(deg)	max	thld	COG	max	thld	COG
5.0	20.0	20.0	20.0	–0.04	0.01	–0.03
10.0	19.9	20.0	20.0	–0.06	0.03	–0.01
15.0	19.9	19.9	19.9	–0.14	–0.06	–0.12
20.0	19.7	19.8	19.8	–0.32	–0.17	–0.23
25.0	19.6	19.7	19.7	–0.38	–0.28	–0.32
30.0	19.5	20.3	19.9	–0.50	0.27	–0.06
35.0	19.2	20.1	19.8	–0.76	0.08	–0.25
40.0	19.2	19.9	19.5	–0.84	–0.14	–0.46
45.0	18.8	19.5	19.2	–1.17	–0.49	–0.75
50.0	18.5	19.0	18.8	–1.52	–1.04	–1.21
55.0	18.3	18.3	18.3	–1.68	–1.66	–1.73
60.0	17.6	18.7	18.3	–2.38	–1.28	–1.75
mean error(cm)				–0.54	–0.39	–0.58
absolute mean error(cm)				0.82	0.46	0.58

Table 3.8: Range estimates and errors for wood at 30 cm when $\phi = 0°$ and $\theta \neq 0°$.

	r estimate(cm)			error(cm)		
θ(deg)	max	thld	COG	max	thld	COG
5.0	29.9	30.1	30.1	–0.10	0.14	0.09
10.0	29.8	30.2	30.1	–0.17	0.16	0.10
15.0	29.8	30.0	29.9	–0.21	–0.04	–0.07
20.0	29.5	30.3	30.1	–0.46	0.34	0.06
25.0	29.3	30.3	29.9	–0.68	0.27	–0.08
30.0	28.9	30.1	29.9	–1.09	0.14	–0.12
35.0	28.6	29.9	29.6	–1.38	–0.06	–0.44
40.0	28.4	29.8	29.3	–1.62	–0.19	–0.74
45.0	28.1	29.5	28.9	–1.88	–0.54	–1.12
50.0	27.5	28.8	28.3	–2.54	–1.20	–1.70
55.0	27.1	27.8	27.5	–2.89	–2.25	–2.49
60.0	26.4	26.9	26.7	–3.59	–3.15	–3.34
mean error(cm)				–1.38	–0.53	–0.82
absolute mean error(cm)				1.38	0.70	0.86

Table 3.9: Range estimates and errors for wood at 40 cm when $\phi = 0°$ and $\theta \neq 0°$.

	r estimate(cm)			error(cm)		
θ(deg)	max	thld	COG	max	thld	COG
5.0	40.0	39.9	39.9	0.02	–0.11	–0.12
10.0	39.9	39.9	39.9	–0.09	–0.11	–0.12
15.0	39.7	39.9	39.9	–0.31	–0.13	–0.15
20.0	39.2	39.7	39.7	–0.83	–0.27	–0.30
25.0	39.2	39.6	39.6	–0.79	–0.40	–0.44
30.0	38.4	39.4	39.3	–1.56	–0.64	–0.72
35.0	38.8	39.1	39.0	–1.19	–0.86	–1.01
40.0	38.2	38.5	38.4	–1.84	–1.47	–1.56
mean error(cm)				–0.82	–0.50	–0.55
absolute mean error(cm)				0.83	0.50	0.55

Table 3.10: Range estimates and errors for white paper at 10 cm when $\phi = 0°$ and $\theta \neq 0°$.

	r estimate(cm)			error(cm)		
θ(deg)	max	thld	COG	max	thld	COG
5.0	9.5	10.0	10.0	–0.47	–0.03	–0.03
10.0	11.0	10.0	10.0	0.96	0.02	0.02
15.0	10.0	10.1	10.1	–0.03	0.08	0.07
20.0	9.2	10.0	10.0	–0.80	0.04	0.03
25.0	9.7	10.2	10.2	–0.29	0.23	0.18
30.0	9.7	10.2	10.1	–0.27	0.19	0.13
35.0	9.0	10.0	10.0	–1.02	0.04	–0.04
40.0	9.3	9.9	9.8	–0.75	–0.05	–0.16
45.0	9.2	9.7	9.6	–0.84	–0.27	–0.38
50.0	9.0	9.6	9.4	–0.99	–0.40	–0.56
55.0	8.8	9.3	9.2	–1.25	–0.66	–0.83
60.0	8.5	9.0	8.8	–1.54	–1.04	–1.18
mean error(cm)				–0.61	–0.15	–0.23
absolute mean error(cm)				0.77	0.25	0.30

Table 3.11: Range estimates and errors for white paper at 20 cm when $\phi = 0°$ and $\theta \neq 0°$.

	r estimate(cm)			error(cm)		
θ(deg)	max	thld	COG	max	thld	COG
5.0	19.8	19.9	19.8	–0.17	–0.12	–0.18
10.0	19.8	19.9	19.9	–0.17	–0.08	–0.14
15.0	19.8	19.9	19.8	–0.21	–0.10	–0.15
20.0	19.6	19.8	19.7	–0.41	–0.21	–0.26
25.0	19.6	19.7	19.7	–0.39	–0.30	–0.33
30.0	19.4	19.4	19.4	–0.62	–0.58	–0.58
35.0	19.3	20.1	19.7	–0.69	0.07	–0.27
40.0	19.1	19.8	19.5	–0.87	–0.23	–0.53
45.0	18.7	19.4	19.1	–1.28	–0.63	–0.88
50.0	18.4	18.9	18.7	–1.61	–1.13	–1.31
55.0	18.0	18.1	18.1	–1.98	–1.88	–1.93
60.0	17.4	18.1	17.9	–2.64	–1.90	–2.08
mean error(cm)				–0.92	–0.59	–0.72
absolute mean error(cm)				0.92	0.60	0.72

Table 3.12: Range estimates and errors for white paper at 30 cm when $\phi = 0°$ and $\theta \neq 0°$.

	r estimate(cm)			error(cm)		
θ(deg)	max	thld	COG	max	thld	COG
5.0	29.5	29.7	29.7	–0.54	–0.32	–0.33
10.0	29.3	29.9	29.8	–0.68	–0.10	–0.18
15.0	29.5	29.9	29.8	–0.46	–0.11	–0.22
20.0	29.4	29.9	29.8	–0.65	–0.08	–0.22
25.0	29.2	29.7	29.6	–0.83	–0.30	–0.42
30.0	29.1	29.7	29.6	–0.90	–0.33	–0.40
35.0	28.8	29.5	29.4	–1.16	–0.46	–0.59
40.0	28.5	29.3	29.1	–1.46	–0.68	–0.86
45.0	28.2	29.1	28.8	–1.75	–0.89	–1.16
50.0	27.6	28.8	28.3	–2.38	–1.22	–1.68
55.0	27.4	28.0	27.6	–2.60	–2.04	–2.35
60.0	26.4	26.7	26.6	–3.61	–3.30	–3.41
mean error(cm)				–1.42	–0.82	–0.99
absolute mean error(cm)				1.42	0.82	0.99

Table 3.13: Range estimates and errors for white paper at 40 cm when $\phi = 0°$ and $\theta \neq 0°$.

	r estimate(cm)			error(cm)		
θ(deg)	max	thld	COG	max	thld	COG
5.0	39.7	39.8	39.8	–0.31	–0.20	–0.24
10.0	39.3	39.8	39.7	–0.66	–0.24	–0.29
15.0	39.2	39.8	39.7	–0.83	–0.24	–0.30
20.0	39.2	39.7	39.6	–0.81	–0.31	–0.41
25.0	39.1	39.5	39.4	–0.90	–0.46	–0.60
30.0	38.7	39.4	39.1	–1.30	–0.62	–0.87
35.0	38.3	39.0	38.7	–1.71	–1.03	–1.27
40.0	38.1	38.2	38.1	–1.93	–1.78	–1.86
mean error(cm)				–1.01	–0.61	–0.73
absolute mean error(cm)				1.01	0.61	0.73

3.2.3 Experimental results when $\phi \neq 0°, \theta = 0°$

In this case, reference data sets are collected for the wooden surface, for ϕ ranging from 5° to 45° with 5° increments. Using these data, ρ values are extracted for corresponding ϕ values as depicted in Figure 3.11 by measuring the actual distance z and evaluating $\rho = \arctan(r/a)$ (Figure 2.9). As the next step, using the same set of data, $(a_2 - a_1)/d$ data is calculated using the procedure explained in Section 2.2 (Figure 3.12). As soon as these two curves ($\tan\rho$ versus ϕ and $(a_2 - a_1)/d$ versus ϕ) are obtained, a new data set is collected to be used as test data. Three different approaches are used.

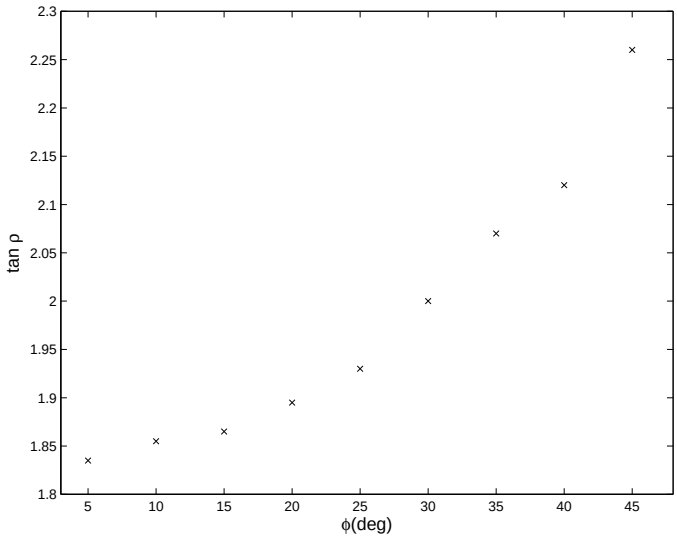

Figure 3.11: Experimental data for $\tan\rho$ versus ϕ.

The first approach is based on linear interpolation on Figures 3.11 and 3.12. First, the $(a_2 - a_1)/d$ value is calculated based on the two positions where maximum intensity is observed. From Figure 3.12, the corresponding ϕ value is estimated by linear interpolation. Then the value of $\tan\rho$ corresponding to this estimated ϕ value is found by a second linear interpolation on Figure 3.11. Finally, the range to the surface is estimated based on Equation (2.4).

In the second approach, instead of using a second linear interpolation to find the value of ρ we find the value of $\tan\rho$ using Equation (2.3).

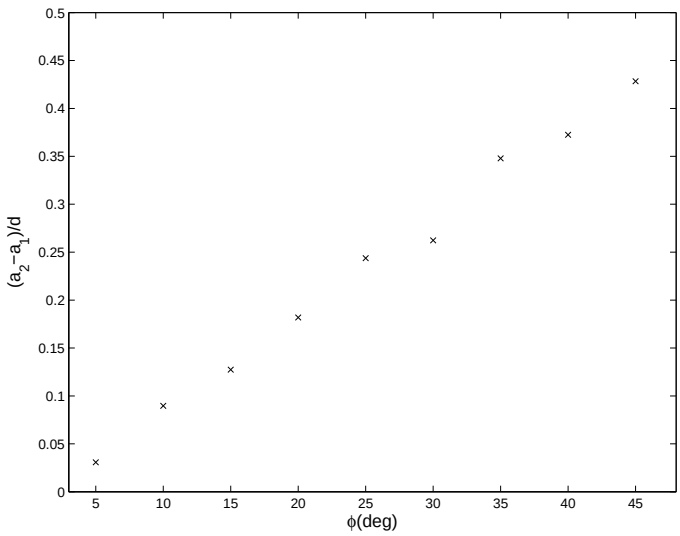

Figure 3.12: Experimental data for $(a_2 - a_1)/d$ versus ϕ.

In the third approach, we use Equation (2.2) as in the $\phi = 0°, \theta = 0°$ case, ignoring the nonzero value of ϕ.

The results are tabulated in Tables 3.14–3.16. Using the first approach, the range and the azimuth angle can be estimated quite accurately. With the second approach, the errors are large for small values of ϕ due to the tan(.) function. This is because the fact that the error in ϕ estimates is of the same order of magnitude for all ϕ values. As the tan(.) values of smaller angles are small, an error in ϕ causes a greater percentage error in the range estimates whereas for larger values of ϕ, this percentage is lower. With the third approach, the range error increases with increasing values of ϕ as expected, since the nonzero value of ϕ is ignored by taking this approach.

Table 3.14: Range errors when $\phi \neq 0°$ and $\theta = 0°$ for the wooden surface by the maximum intensity method.

ϕ(deg)			true	range error(cm)		
true	estimate	error	r(cm)	method 1	method 2	method 3
5	7	2	32.8	–0.27	5.27	–0.36
5	7	2	33.4	–0.36	5.27	–0.45
10	10	0	37.9	–0.44	4.57	–0.57
10	10	0	39.0	–0.59	4.43	–0.82
15	16	1	29.3	–0.68	1.75	–1.09
15	16	1	31.5	–0.34	2.30	–0.79
20	21	1	30.3	–0.20	2.05	–1.13
20	21	1	33.1	–0.11	2.36	–1.14
25	25	0	28.7	–0.99	2.25	–2.29
25	25	0	32.3	–1.03	2.61	–2.51
30	31	1	28.8	–1.87	–0.84	–4.21
30	31	1	33.9	–0.95	0.31	–3.81
35	33	2	30.1	–0.90	–1.94	–3.80
35	33	2	36.7	–1.43	–2.70	–4.94
40	42	2	17.8	–1.28	–0.43	–3.86
40	42	2	26.4	–0.76	0.54	–4.77
45	49	4	12.5	–0.12	0.05	–2.94
45	49	4	24.8	–0.10	0.25	–5.71
mean error(cm)				–0.69	1.56	–2.51
absolute mean error(cm)				0.69	2.22	2.51

Table 3.15: Range errors when $\phi \neq 0^\circ$ and $\theta = 0^\circ$ for the wooden surface by the thresholding method.

ϕ(deg)			true	range error(cm)		
true	estimate	error	r(cm)	method 1	method 2	method 3
5	7	2	32.8	–0.07	5.50	–0.16
5	7	2	33.4	0.03	5.72	–0.06
10	10	0	37.9	–0.10	4.84	–0.33
10	10	0	39.0	–0.13	4.95	–0.36
15	16	1	29.3	0.09	2.58	–0.34
15	16	1	31.5	–0.17	2.48	–0.62
20	21	1	30.3	0.07	2.34	–0.88
20	21	1	33.1	0.04	2.52	–0.99
25	25	0	28.7	0.25	3.63	–1.11
25	25	0	32.3	0.01	3.77	–1.52
30	31	1	28.8	0.44	1.56	–2.10
30	31	1	33.9	0.46	1.77	–2.53
35	33	2	30.1	0.06	–1.02	–2.94
35	33	2	36.7	–0.21	–1.51	–3.84
40	42	2	17.8	0.77	1.72	–2.13
40	42	2	26.4	1.09	2.49	–3.21
45	49	4	12.5	0.42	0.60	–2.51
45	49	4	24.8	1.76	2.13	–4.28
mean error(cm)				0.27	2.56	–1.66
absolute mean error(cm)				0.34	2.84	1.66

Table 3.16: Range errors when $\phi \neq 0°$ and $\theta = 0°$ for the wooden surface by the COG method.

ϕ(deg)			true	range error(cm)		
true	estimate	error	r(cm)	method 1	method 2	method 3
5	7	2	32.8	–0.09	5.48	–0.18
5	7	2	33.4	0.01	5.70	–0.08
10	10	0	37.9	–0.14	4.80	–0.37
10	10	0	39.0	–0.15	4.93	–0.38
15	16	1	29.3	–0.04	2.44	–0.46
15	16	1	31.5	–0.21	2.44	–0.66
20	21	1	30.3	–0.03	2.24	–0.97
20	21	1	33.1	–0.02	2.46	–1.05
25	25	0	28.7	0.02	3.37	–1.34
25	25	0	32.3	–0.09	3.67	–1.61
30	31	1	28.8	0.14	1.25	–2.37
30	31	1	33.9	0.12	1.42	–2.84
35	33	2	30.1	–0.14	–1.21	–3.12
35	33	2	36.7	–0.56	–1.85	–4.15
40	42	2	17.8	–0.19	0.71	–2.94
40	42	2	26.4	0.57	1.94	–3.65
45	49	4	12.5	0.33	0.51	–2.59
45	49	4	24.8	1.40	1.77	–4.55
mean error(cm)				0.05	2.34	–1.85
absolute mean error(cm)				0.24	2.68	1.85

3.2.4 Experimental results when $\phi \neq 0°, \theta \neq 0°$

Finally, to see the effects of θ when $\phi \neq 0°$, we collected reference data sets for the wooden surface for θ ranging from 5° to 25° with 5° increments for three values of ϕ, which are 5°, 10°, and 15°. The range estimates are made using the first approach in the previous section, since the value of θ is not effective in range estimation. The results obtained are given in Table 3.17. When the error values are investigated, it is seen that the overall accuracy here is of the same order of magnitude as that of $\phi \neq 0°, \theta = 0°$ case. However, remember that in the $\phi = 0°, \theta \neq 0°$ case, the error values tend to increase with increasing values of θ. Therefore, it can be concluded that when both $\phi \neq 0°$ and $\theta \neq 0°$, the effects of θ being non-zero is dominated by the effects introduced by the non-zero value of ϕ. As the effects caused by non-zero ϕ value is compensated by the procedure followed, range estimates in this case are very successful despite the effects of non-zero θ.

As expected, the maximum intensity values for this case are smaller than the values for the other cases of the same range. This is a natural result of the fact that for this case, a smaller percentage of the reflected light reaches the detector due to nonzero values of ϕ and θ. However, when the intensity plots are investigated, the slopes of the rising and falling edges differ obviously as in the $\phi \neq 0°, \theta = 0°$ case. Therefore, in $\phi \neq 0°$ cases, the decision of θ being zero or not needs more computing or additional data. One way to handle this situation would be to use a second detector moving perpendicularly to the first one, from which additional data regarding θ could be obtained.

When all of the results from different cases are considered, it can be concluded that the errors in the estimates are comparable with the precision of the actual range, that is the main source of the errors is the uncertainty in the actual range measurements. However, a second dominating source of error is the precision of the analog output of the infrared sensors, which is a natural result of the beamwidth of the light emitted. Considering these limitations, it seems that this study has reached the limit precision allowed by the infrared sensors we used.

Table 3.17: Range errors when $\phi \neq 0°$ and $\theta \neq 0°$ for the wooden surface.

ϕ(deg)	θ(deg)	true r(cm)	error(cm) max	thld	COG
5	5	31.0	–0.06	0.27	0.23
5	10	33.1	–1.12	–0.03	0.05
5	15	35.1	–0.56	–0.3	–0.06
5	20	36.5	–0.21	0.10	0.09
5	25	39.0	–0.29	0.02	–0.05
10	5	30.5	–0.20	0.47	0.37
10	10	33.0	–0.37	0.04	–0.02
10	15	35.0	–0.26	0.28	0.22
10	20	36.5	–0.13	0.20	0.11
10	25	38.5	–0.32	0.00	–0.02
15	5	29.5	–0.09	0.39	0.24
15	10	31.5	0.00	0.35	0.33
15	15	34.0	0.00	0.86	0.76
15	20	37.0	–0.95	–0.30	–0.35
15	25	38.5	–0.71	0.31	0.10
mean error(cm)			–0.35	0.18	0.13
absolute mean error(cm)			0.35	0.26	0.20

Chapter 4

CONCLUSIONS and FUTURE WORK

In this study, a novel method for position estimation of surfaces with infrared sensors has been described. We use a pair of infrared sensors mounted on a vertical linear platform on which they can be moved independently. The basic idea of our method is that, while the sensors are being moved, the detector reading is maximum at some positions and the corresponding positional values of the sensors can be used for range estimation with suitable processing of the infrared intensity signals. To realize this idea, the detector slides along the platform to collect intensity data and these data are compared to find the maximum in magnitude for a given position of the emitter. Possible localization schemes have been investigated separately using three different ways of processing the infrared intensity signals. For all cases, the behavior of the proposed system has been carefully investigated to formulate the actual range of the targets involved. The processing method which gives the most accurate results is based on finding the center of gravity of the infrared intensity scans. In this case, the best absolute range error achieved by the system is calculated as 0.15 cm over the range from 10 to 50 cm.

The method is expanded for cases where the azimuth angle θ and the elevation

angle ϕ are nonzero. A new technique is developed for the case where ϕ is nonzero. The system performance for these cases is investigated using different approaches.

The experimental results obtained show that the model is successful in localizing objects to an unexpectedly high accuracy without prior knowledge of the surface characteristics. Thus, considering the fast response time and high accuracy obtained experimentally, the system developed can be used for real-time range estimation in mobile robot applications.

The main contribution of this thesis is that the method we develop is relatively independent of the type of surface encountered since it is based on searching the maximum value of the intensity rather than using absolute intensity values for a given surface which would depend on the surface type. The system can be viewed as a triangulation system tuned for maximum intensity data. As long as intensity data are available over a given range of detector positions, range is estimated relatively independently of surface type.

Our current and future work involves improving of the system performance when the azimuth angle θ is nonzero. Moreover, estimating the value of θ angle in any case will enable our system to be used in map building of unknown indoor environments. One way to increase the accuracy of angular position estimation would be to include a second detector in the system moving perpendicularly to the first one. This would add an additional dimension to the present system.

In this study, we considered range estimation to planar walls. A related future research direction is to extend the range estimation method developed here to other geometries frequently encountered in indoor environments such as corners, edges, and cylinders. Recognition of different surface types or discontinuities in the surface characteristics is another problem to address.

Bibliography

[1] A. M. Flynn, "Combining sonar and infrared sensors for mobile robot navigation," *International Journal of Robotics Research*, vol. 7, pp. 5–14, December 1988.

[2] P. J. Phillips, "Matching pursuit filters applied to face identification," *IEEE Transactions on Image Processing*, vol. 7, pp. 1150–1164, August 1998.

[3] H. Kwon, S. Z. Der, and N. M. Nasrabadi, "Adaptive multisensor target detection using feature-based fusion," *Optical Engineering*, vol. 41, pp. 69–80, January 2002.

[4] T. Tsao and Z. Q. Wen, "Image-based target tracking through rapid sensor orientation change," *Optical Engineering*, vol. 41, pp. 697–703, March 2002.

[5] I. Pavlidis, P. Symosek, B. Fritz, M. Bazakos, and N. Papanikolopoulos, "Automatic detection of vehicle occupants: the imaging problem and its solution," *Machine Vision and Applications*, vol. 11, pp. 313–320, April 2000.

[6] P. M. Tag, R. L. Bankert, and L. R. Brody, "An AVHRR multiple cloud-type classification package," *Journal of Applied Meteorology*, vol. 39, pp. 125–134, February 2000.

[7] A. K. Jain, N. K. Ratha, and S. Lakshmanan, "Object detection using Gabor filters," *Pattern Recognition*, vol. 30, pp. 295–309, February 1997.

[8] Z. Zalevsky, D. Mendlovic, E. Rivlin, and S. Rotman, "Contrasted statistical processing algorithm for obtaining improved target detection performances

in infrared cluttered environment," *Optical Engineering*, vol. 39, pp. 2609–2617, October 2000.

[9] B. Bhanu, P. Symosek, and S. Das, "Analysis of terrain using multispectral images," *Pattern Recognition*, vol. 30, pp. 197–215, February 1997.

[10] K. Hashimoto, C. Kawaguchi, S. Matsueda, K. Morinaka, and N. Yoshiike, "People counting system using multisensing application," *Sensors and Actuators A—Physical*, vol. 66, pp. 50–55, 1 April 1998.

[11] A. J. Hand, "Infrared sensor counts insects," *Photonics Spectra*, vol. 32, pp. 30–31, November 1998.

[12] H. C. Wikle, S. Kottilingam, R. H. Zee, and B. A. Chin, "Infrared sensing techniques for penetration depth control of the submerged arc welding process," *Journal of Materials Processing Technology*, vol. 113, pp. 228–233, 15 June 2001.

[13] B. Butkiewicz, "Position control system with fuzzy microprocessor AL220," *Lecture Notes in Computer Science*, vol. 1226, pp. 74–81, 1997.

[14] H. R. Everett, *Sensors for Mobile Robots, Theory and Application.* 289 Linden St, Wellesley, MA: A K Peters, Ltd., 1995.

[15] G. Beccari, S. Caselli, and F. Zanichelli, "Qualitative spatial representations from task-oriented perception and exploratory behaviors," *Robotics and Autonomous Systems*, vol. 25, pp. 147–157, 30 November 1998.

[16] A. Warszawski, Y. Rosenfeld, and I. Shohet, "Autonomous mapping system for an interior finishing robot," *Journal of Computing in Civil Engineering*, vol. 10, pp. 67–77, January 1996.

[17] E. P. Lopes, E. P. L. Aude, J. T. C. Silveria, H. Serderia, and M. F. Martins, "Application of a blind person strategy for obstacle avoidance with the use of potential fields," in *Proceedings of IEEE International Conference on Robotics and Automation*, vol. 3, pp. 2911–2916, Seoul, South Korea, 21–26 May 2001.

[18] H. M. Barberá, A. G. Skarmeta, M. Z. Izquierdo, and J. B. Blaya, "Neural networks for sonar and infrared sensors fusion," in *Proceedings of the Third International Conference on Information Fusion*, vol. 2, pp. 18–25, France, 10–13 July 2000.

[19] A. M. Sabatini, V. Genovese, E. Guglielmelli, A. Mantuano, G. Ratti, and P. Dario, "A low-cost, composite sensor array combining ultrasonic and infrared proximity sensors," in *Proceedings of the IEEE/RSJ International Conference on Intelligent Robots and Systems*, pp. 120–126, Pittsburgh, PA, 5–9 August 1995.

[20] B. Chen and J. K. Tugnait, "Multisensor tracking of a maneuvering target in clutter using IMMPDA fixed-lag smoothing," *IEEE Transactions on Aerospace and Electronic Systems*, vol. 36, pp. 983–991, July 2000.

[21] Y. M. Chen and H. C. Huang, "Fuzzy logic approach to multisensor data association," *Mathematics and Computers in Simulation*, vol. 52, pp. 399–412, 15 July 2000.

[22] E. Cheung and V. J. Lumelsky, "Proximity sensing in robot manipulator motion planning: system and implementation issues," *IEEE Transactions on Robotics and Automation*, vol. 5, pp. 740–751, December 1989.

[23] V. J. Lumelsky and E. Cheung, "Real-time collision avoidance in teleoperated whole-sensitive robot arm manipulators," *IEEE Transactions on Systems Man and Cybernetics*, vol. 23, pp. 194–203, January/February 1993.

[24] P. M. Novotny and N. J. Ferrier, "Using infrared sensors and the Phong illumination model to measure distances," in *Proceedings of IEEE International Conference on Robotics and Automation*, pp. 1644–1649, Detroit, MI, 10–15 May 1999.

[25] B. T. Phong, "Illumination for computer generated pictures," *Communications of the ACM*, vol. 18, pp. 311–317, June 1975.

[26] B. Andò and S. Graziani, "A new IR displacement system based on noise added theory," in *Proceedings of the 18th IEEE Instrumentation and Measurement Technology Conference*, pp. 482–485, Budapest, Hungary, 21–23 May 2001.

[27] L. Korba, S. Elgazzar, and T. Welch, "Active infrared sensors for mobile robots," *IEEE Transactions on Instrumentation and Measurement*, vol. 43, pp. 283–287, April 1994.

[28] K. Hashimoto, T. Tsuruta, K. Morinaka, and N. Yoshiike, "High performance human information sensor," *Sensors and Actuators A—Physical*, vol. 79, pp. 46–52, 25 January 2000.

[29] N. Yoshiike, K. Morinaka, K. Hashimoto, M. Kawaguri, and S. Tanaka, "360 degrees direction type human information sensor," *Sensors and Actuators A—Physical*, vol. 77, pp. 199–208, 2 November 1999.

[30] P. J. de Groot, G. J. Postma, W. J. Melssen, and L. M. C. Buydens, "Validation of remote, on-line, near-infrared measurements for the classification of demolition waste," *Analytica Chemica Acta*, vol. 453, pp. 117–124, 18 February 2002.

[31] D. M. Scott, "A 2-color near-infrared sensor for sorting recycled plastic waste," *Measurement Science and Technology*, vol. 6, pp. 156–159, February 1995.

[32] G. Benet, F. Blanes, J. E. Simó, and P. Pérez, "Using infrared sensors for distance measurement in mobile robots," *Robotics and Autonomous Systems*, vol. 40, pp. 255–266, September 2002.

[33] T. Aytaç and B. Barshan, "Differentiation and localization of targets using infrared sensors," *Optics Communications*, vol. 210, pp. 25–35, September 2002.

[34] T. Aytaç and B. Barshan, "Rule-based target differentiation and position estimation based on infrared intensity measurements," *Optical Engineering*, vol. 42, pp. 1766–1771, June 2003.

[35] B. Barshan and T. Aytaç, "Position-invariant surface recognition and localization using infrared sensors," *Optical Engineering*, vol. 42, pp. 3589–3594, December 2003.

[36] M. Born, and E. Wolf, *Principles of Optics*. Oxford, UK: Pergamon Press, 1980.

[37] Matrix Elektronik, AG, Kirchweg 24 CH-5422 Oberehrendingen, Switzerland, *IRS-U-4A Proximity Switch Datasheet*, 1995.

Appendix A

Proof showing that ρ is dependent only on ϕ and β

Using Figure (2.9),

$$b = \frac{l}{\tan(\gamma + \beta)} \tag{A.1}$$

$$x = \frac{l}{\tan \phi} \tag{A.2}$$

$$b = m \cos(\gamma + \beta) \tag{A.3}$$

by the sine law,

$$\frac{2a}{\sin\Big[180 - (2\gamma + \beta)\Big]} = \frac{m}{\sin \gamma} \tag{A.4}$$

then,

$$m = \frac{2a \sin\gamma}{\sin\Big[180 - (2\gamma + \beta)\Big]} \tag{A.5}$$

combining Equations (A.3) and (A.5),

$$b = \frac{2a \sin\gamma \cos(\gamma + \beta)}{\sin\Big[180 - (2\gamma + \beta)\Big]} \tag{A.6}$$

$$c = a - b \tag{A.7}$$

$$\tan\rho = \frac{r}{a} \tag{A.8}$$

using Equations (A.1) and (A.6),

$$a = \frac{l \sin\Big[180 - (2\gamma + \beta)\Big]}{2 \sin\gamma \cos(\gamma + \beta) \tan(\gamma + \beta)} \tag{A.9}$$

by Equations (A.1) and (A.9),

$$c = \frac{l}{\tan(\gamma + \beta)} \left(\frac{\sin\Big[180 - (2\gamma + \beta)\Big]}{2 \sin\gamma \cos(\gamma + \beta)} - 1 \right) \tag{A.10}$$

by Figure 2.9,

$$r = (x + c) \tan\phi \tag{A.11}$$

$$r = l + c \tan\phi \tag{A.12}$$

combining Equations (A.10) and (A.12),

$$r = l + \tan\phi \frac{l}{\tan(\gamma+\beta)} \left(\frac{\sin\left[180 - (2\gamma+\beta)\right]}{2\sin\gamma\cos(\gamma+\beta)} - 1 \right) \tag{A.13}$$

substituting z in Equation (A.8),

$$\tan\rho = \frac{l\left(1 + \frac{\tan\phi}{\tan(\gamma+\beta)}\left(\frac{\sin[180-(2\gamma+\beta)]}{2\sin\gamma\cos(\gamma+\beta)} - 1\right)\right)}{l\frac{\sin[180-(2\gamma+\beta)]}{2\sin\gamma\cos(\gamma+\beta)\tan(\gamma+\beta)}} \tag{A.14}$$

in the final form, Equation (A.14) simplifies to,

$$\tan\rho = \frac{1 + \frac{\tan\phi}{\tan(\gamma+\beta)}\left(\frac{\sin[180-(2\gamma+\beta)]}{2\sin\gamma\cos(\gamma+\beta)} - 1\right)}{\frac{\sin[180-(2\gamma+\beta)]}{2\sin\gamma\cos(\gamma+\beta)\tan(\gamma+\beta)}} \tag{A.15}$$

Hence, Equation (A.15) verifies that ρ is dependent only on ϕ and β. This enables us to use ρ and r instead of l for range estimation.

Appendix B

Data sheets of the components

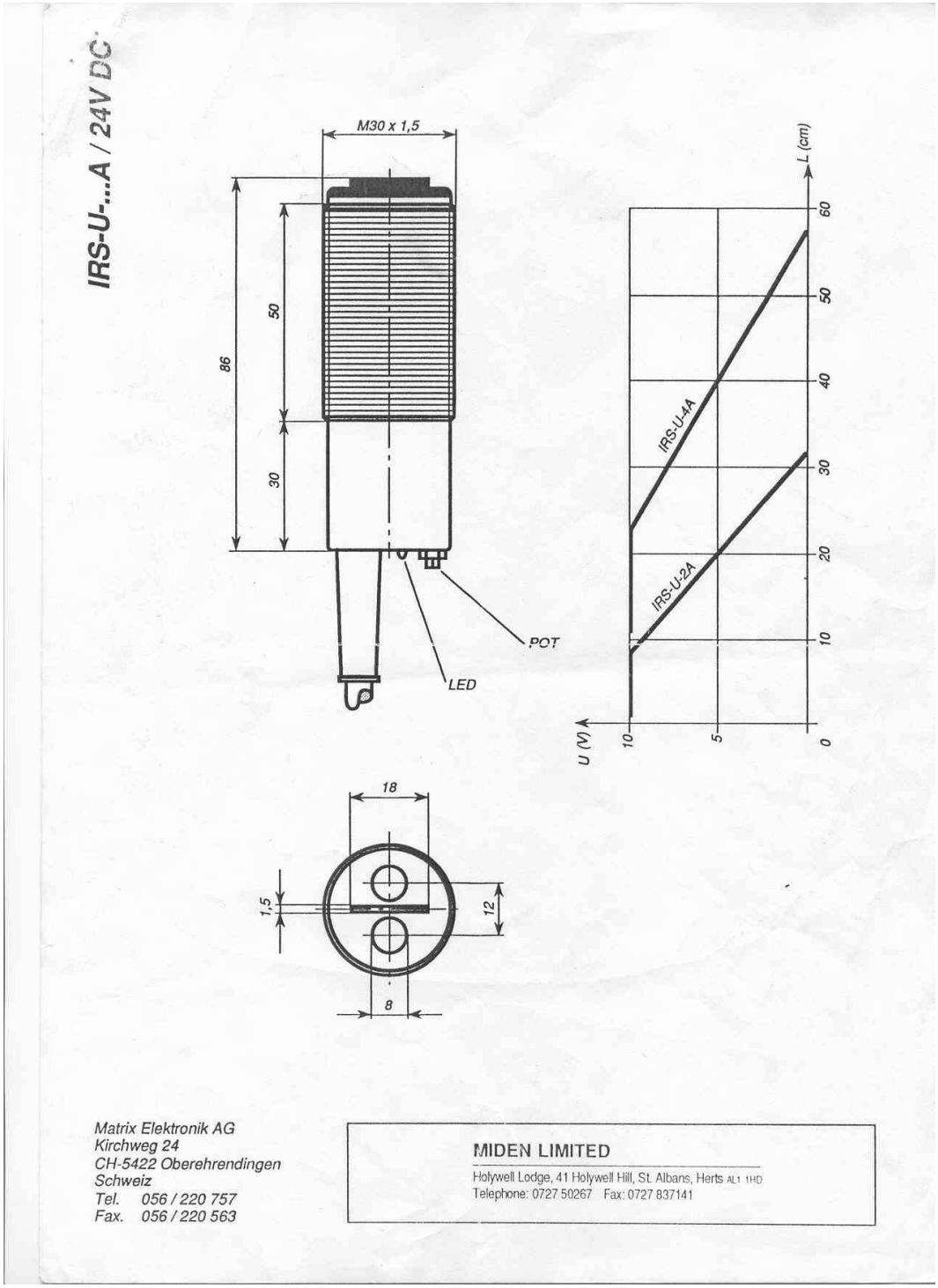

Figure B.1: The datasheet of the infrared sensor used in this study.

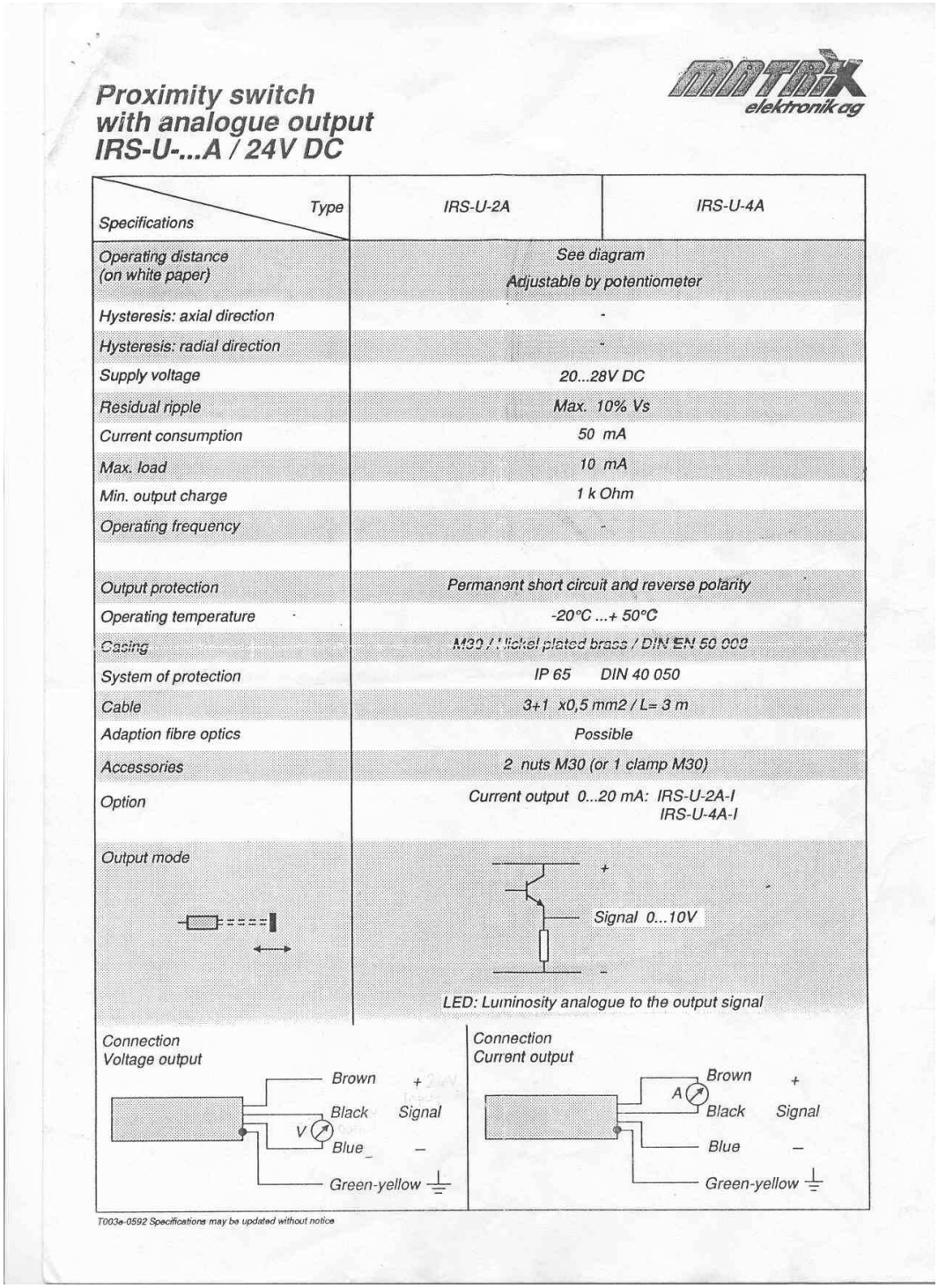

Proximity switch with analogue output IRS-U-...A / 24V DC

matrix elektronik ag

Specifications \ Type	IRS-U-2A	IRS-U-4A
Operating distance (on white paper)	See diagram Adjustable by potentiometer	
Hysteresis: axial direction	-	
Hysteresis: radial direction	-	
Supply voltage	20...28V DC	
Residual ripple	Max. 10% Vs	
Current consumption	50 mA	
Max. load	10 mA	
Min. output charge	1 k Ohm	
Operating frequency	-	
Output protection	Permanent short circuit and reverse polarity	
Operating temperature	-20°C ...+ 50°C	
Casing	M30 / Nickel plated brass / DIN EN 50 002	
System of protection	IP 65 DIN 40 050	
Cable	3+1 x0,5 mm2 / L= 3 m	
Adaption fibre optics	Possible	
Accessories	2 nuts M30 (or 1 clamp M30)	
Option	Current output 0...20 mA: IRS-U-2A-I IRS-U-4A-I	
Output mode	+ Signal 0...10V – LED: Luminosity analogue to the output signal	

Connection Voltage output

Connection Current output

T003a-0592 Specifications may be updated without notice

Figure B.2: The datasheet of the infrared sensor used in this study.

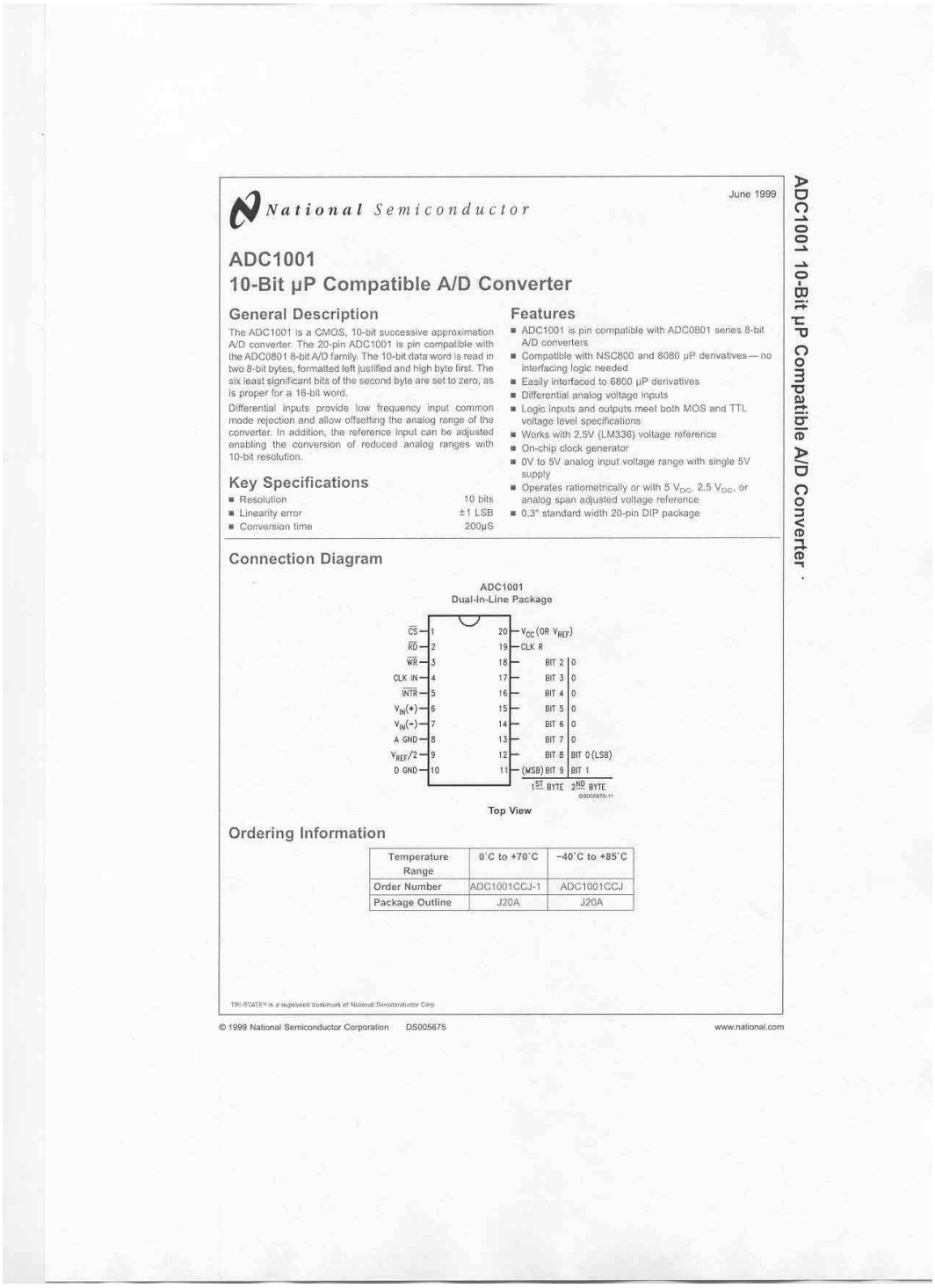

National Semiconductor

June 1999

ADC1001
10-Bit µP Compatible A/D Converter

ADC1001 10-Bit µP Compatible A/D Converter

General Description

The ADC1001 is a CMOS, 10-bit successive approximation A/D converter. The 20-pin ADC1001 is pin compatible with the ADC0801 8-bit A/D family. The 10-bit data word is read in two 8-bit bytes, formatted left justified and high byte first. The six least significant bits of the second byte are set to zero, as is proper for a 16-bit word.

Differential inputs provide low frequency input common mode rejection and allow offsetting the analog range of the converter. In addition, the reference input can be adjusted enabling the conversion of reduced analog ranges with 10-bit resolution.

Features

- ADC1001 is pin compatible with ADC0801 series 8-bit A/D converters
- Compatible with NSC800 and 8080 µP derivatives — no interfacing logic needed
- Easily interfaced to 6800 µP derivatives
- Differential analog voltage inputs
- Logic inputs and outputs meet both MOS and TTL voltage level specifications
- Works with 2.5V (LM336) voltage reference
- On-chip clock generator
- 0V to 5V analog input voltage range with single 5V supply
- Operates ratiometrically or with 5 V_{DC}, 2.5 V_{DC}, or analog span adjusted voltage reference
- 0.3" standard width 20-pin DIP package

Key Specifications

Resolution	10 bits
Linearity error	±1 LSB
Conversion time	200µS

Connection Diagram

ADC1001
Dual-In-Line Package

Top View

Ordering Information

Temperature Range	0°C to +70°C	−40°C to +85°C
Order Number	ADC1001CCJ-1	ADC1001CCJ
Package Outline	J20A	J20A

TRI-STATE® is a registered trademark of National Semiconductor Corp

© 1999 National Semiconductor Corporation DS005675 www.national.com

Figure B.3: The datasheet of the A/D converter used in this study.

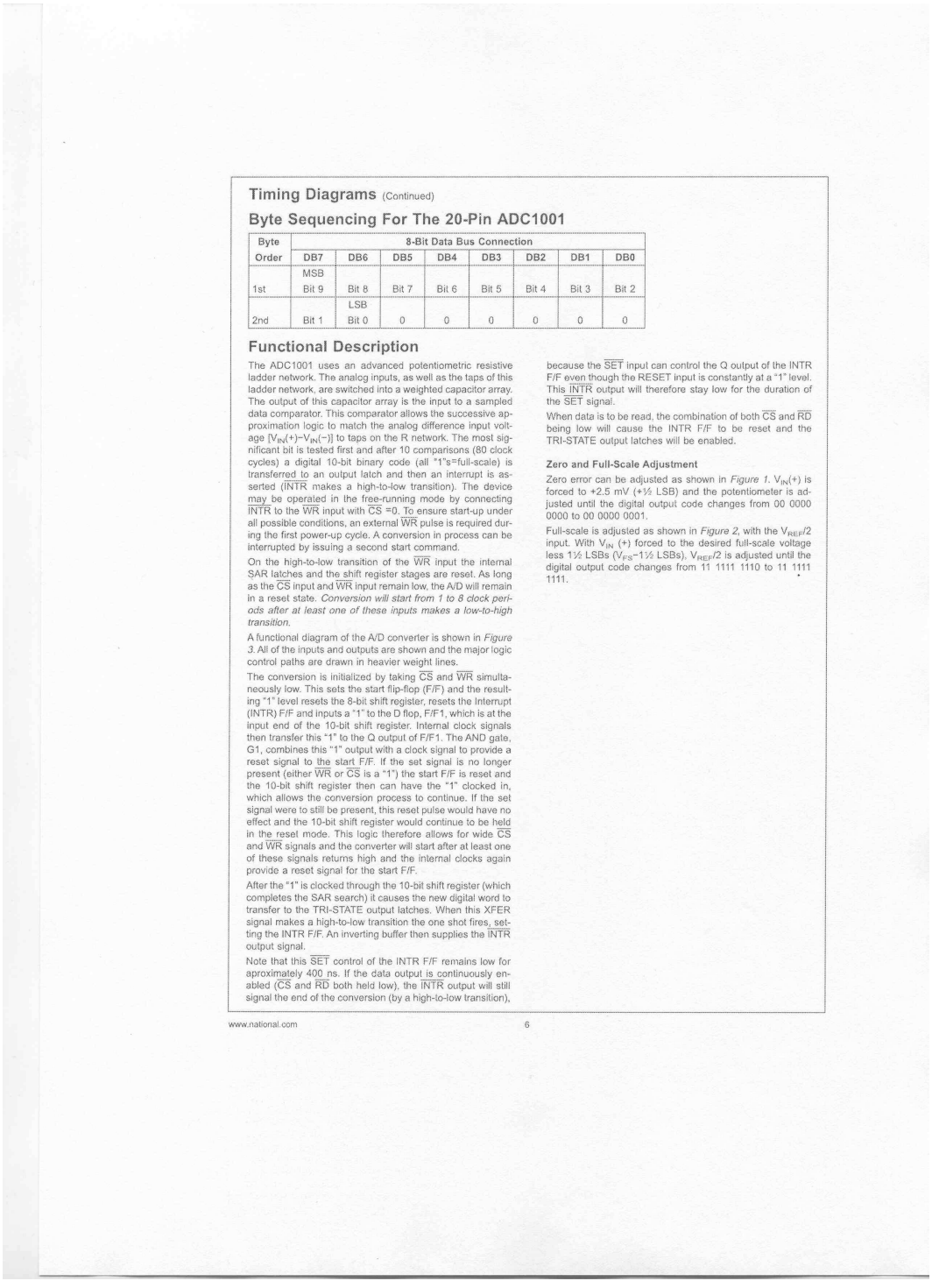

Timing Diagrams (Continued)

Byte Sequencing For The 20-Pin ADC1001

Byte Order	8-Bit Data Bus Connection							
	DB7	DB6	DB5	DB4	DB3	DB2	DB1	DB0
1st	MSB Bit 9	Bit 8	Bit 7	Bit 6	Bit 5	Bit 4	Bit 3	Bit 2
2nd	Bit 1	LSB Bit 0	0	0	0	0	0	0

Functional Description

The ADC1001 uses an advanced potentiometric resistive ladder network. The analog inputs, as well as the taps of this ladder network, are switched into a weighted capacitor array. The output of this capacitor array is the input to a sampled data comparator. This comparator allows the successive approximation logic to match the analog difference input voltage [$V_{IN}(+)-V_{IN}(-)$] to taps on the R network. The most significant bit is tested first and after 10 comparisons (80 clock cycles) a digital 10-bit binary code (all "1"s=full-scale) is transferred to an output latch and then an interrupt is asserted ($\overline{INTR}$ makes a high-to-low transition). The device may be operated in the free-running mode by connecting $\overline{INTR}$ to the $\overline{WR}$ input with $\overline{CS}$ =0. To ensure start-up under all possible conditions, an external $\overline{WR}$ pulse is required during the first power-up cycle. A conversion in process can be interrupted by issuing a second start command.

On the high-to-low transition of the $\overline{WR}$ input the internal SAR latches and the shift register stages are reset. As long as the $\overline{CS}$ input and $\overline{WR}$ input remain low, the A/D will remain in a reset state. *Conversion will start from 1 to 8 clock periods after at least one of these inputs makes a low-to-high transition.*

A functional diagram of the A/D converter is shown in *Figure 3*. All of the inputs and outputs are shown and the major logic control paths are drawn in heavier weight lines.

The conversion is initialized by taking $\overline{CS}$ and $\overline{WR}$ simultaneously low. This sets the start flip-flop (F/F) and the resulting "1" level resets the 8-bit shift register, resets the Interrupt (INTR) F/F and inputs a "1" to the D flop, F/F1, which is at the input end of the 10-bit shift register. Internal clock signals then transfer this "1" to the Q output of F/F1. The AND gate, G1, combines this "1" output with a clock signal to provide a reset signal to the start F/F. If the set signal is no longer present (either $\overline{WR}$ or $\overline{CS}$ is a "1") the start F/F is reset and the 10-bit shift register then can have the "1" clocked in, which allows the conversion process to continue. If the set signal were to still be present, this reset pulse would have no effect and the 10-bit shift register would continue to be held in the reset mode. This logic therefore allows for wide $\overline{CS}$ and $\overline{WR}$ signals and the converter will start after at least one of these signals returns high and the internal clocks again provide a reset signal for the start F/F.

After the "1" is clocked through the 10-bit shift register (which completes the SAR search) it causes the new digital word to transfer to the TRI-STATE output latches. When this XFER signal makes a high-to-low transition the one shot fires, setting the INTR F/F. An inverting buffer then supplies the $\overline{INTR}$ output signal.

Note that this $\overline{SET}$ control of the INTR F/F remains low for aproximately 400 ns. If the data output is continuously enabled ($\overline{CS}$ and $\overline{RD}$ both held low), the $\overline{INTR}$ output will still signal the end of the conversion (by a high-to-low transition), because the $\overline{SET}$ input can control the Q output of the INTR F/F even though the RESET input is constantly at a "1" level. This $\overline{INTR}$ output will therefore stay low for the duration of the $\overline{SET}$ signal.

When data is to be read, the combination of both $\overline{CS}$ and $\overline{RD}$ being low will cause the INTR F/F to be reset and the TRI-STATE output latches will be enabled.

Zero and Full-Scale Adjustment

Zero error can be adjusted as shown in *Figure 1*. $V_{IN}(+)$ is forced to +2.5 mV (+½ LSB) and the potentiometer is adjusted until the digital output code changes from 00 0000 0000 to 00 0000 0001.

Full-scale is adjusted as shown in *Figure 2*, with the $V_{REF}/2$ input. With V_{IN} (+) forced to the desired full-scale voltage less 1½ LSBs (V_{FS}–1½ LSBs), $V_{REF}/2$ is adjusted until the digital output code changes from 11 1111 1110 to 11 1111 1111.

Figure B.4: The datasheet of the A/D converter used in this study.

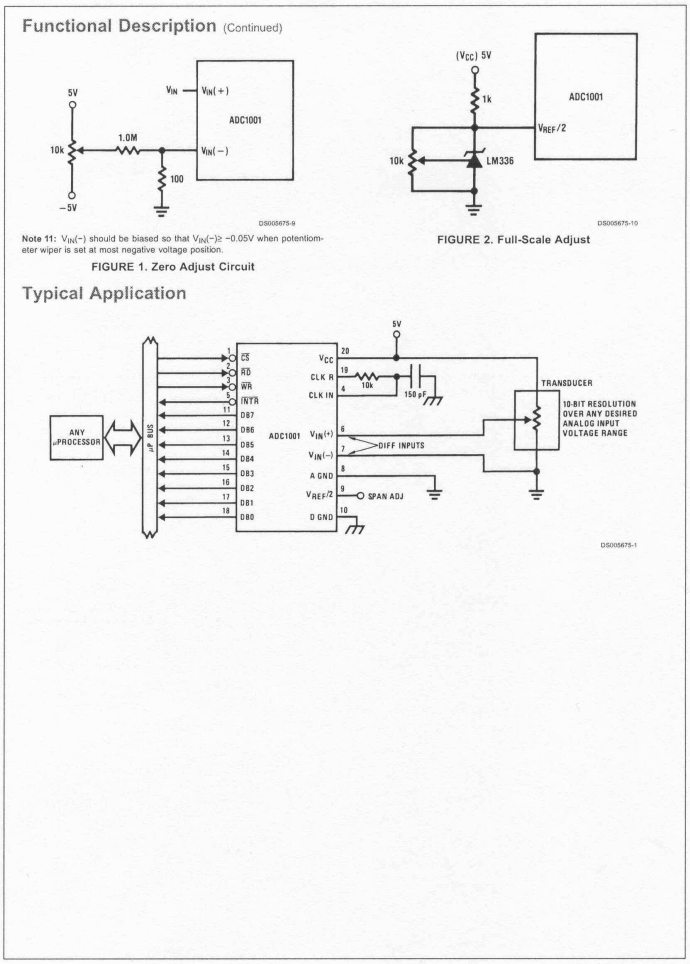

Figure B.5: The datasheet of the A/D converter used in this study.

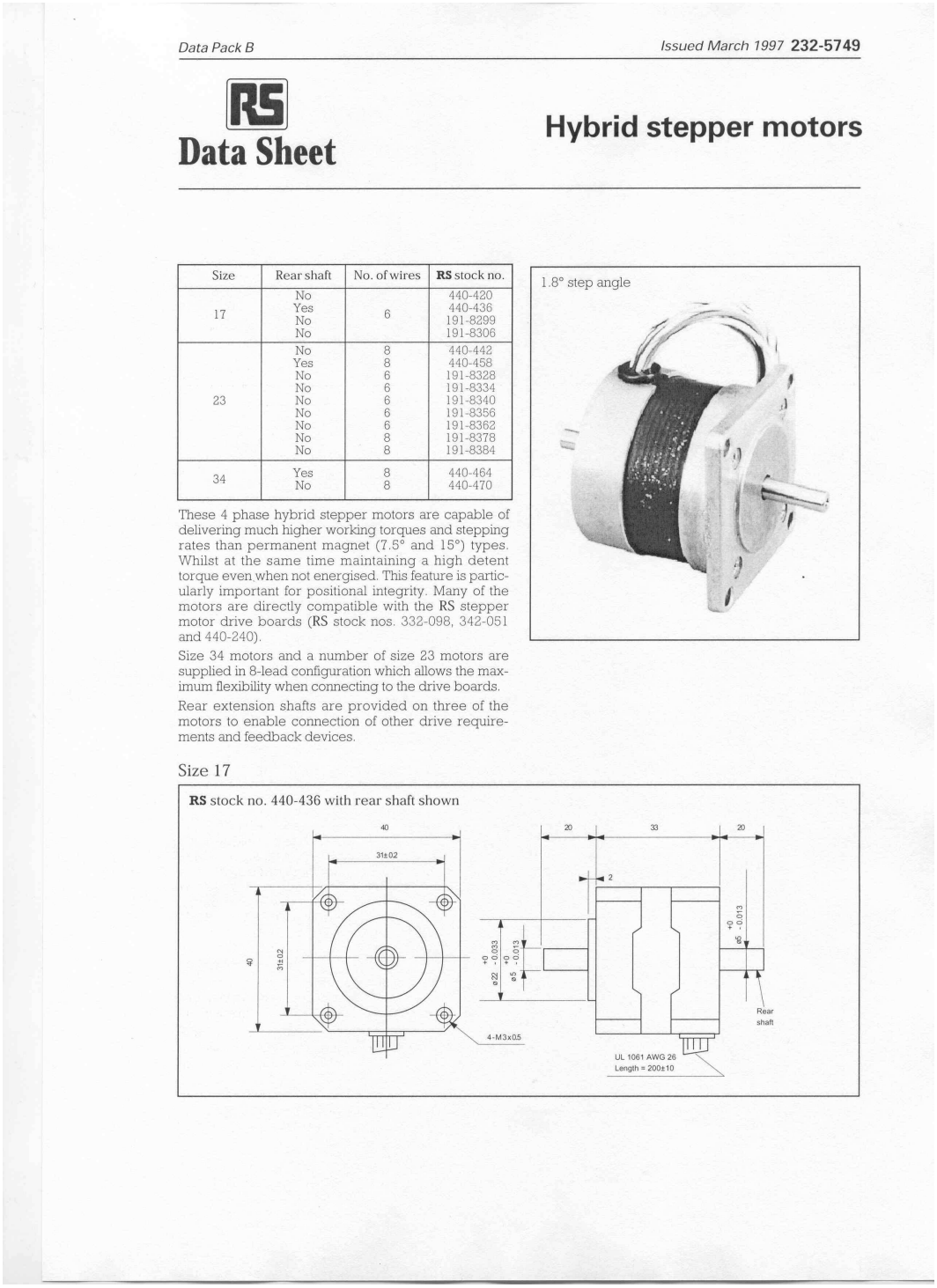

Data Pack B — Issued March 1997 232-5749

RS Data Sheet

Hybrid stepper motors

Size	Rear shaft	No. of wires	RS stock no.
17	No	6	440-420
	Yes		440-436
	No		191-8299
	No		191-8306
23	No	8	440-442
	Yes	8	440-458
	No	6	191-8328
	No	6	191-8334
	No	6	191-8340
	No	6	191-8356
	No	6	191-8362
	No	8	191-8378
	No	8	191-8384
34	Yes	8	440-464
	No	8	440-470

1.8° step angle

These 4 phase hybrid stepper motors are capable of delivering much higher working torques and stepping rates than permanent magnet (7.5° and 15°) types. Whilst at the same time maintaining a high detent torque even when not energised. This feature is particularly important for positional integrity. Many of the motors are directly compatible with the RS stepper motor drive boards (RS stock nos. 332-098, 342-051 and 440-240).

Size 34 motors and a number of size 23 motors are supplied in 8-lead configuration which allows the maximum flexibility when connecting to the drive boards.

Rear extension shafts are provided on three of the motors to enable connection of other drive requirements and feedback devices.

Size 17

RS stock no. 440-436 with rear shaft shown

Figure B.6: The datasheet of the stepper motor used to drive the linear platform.

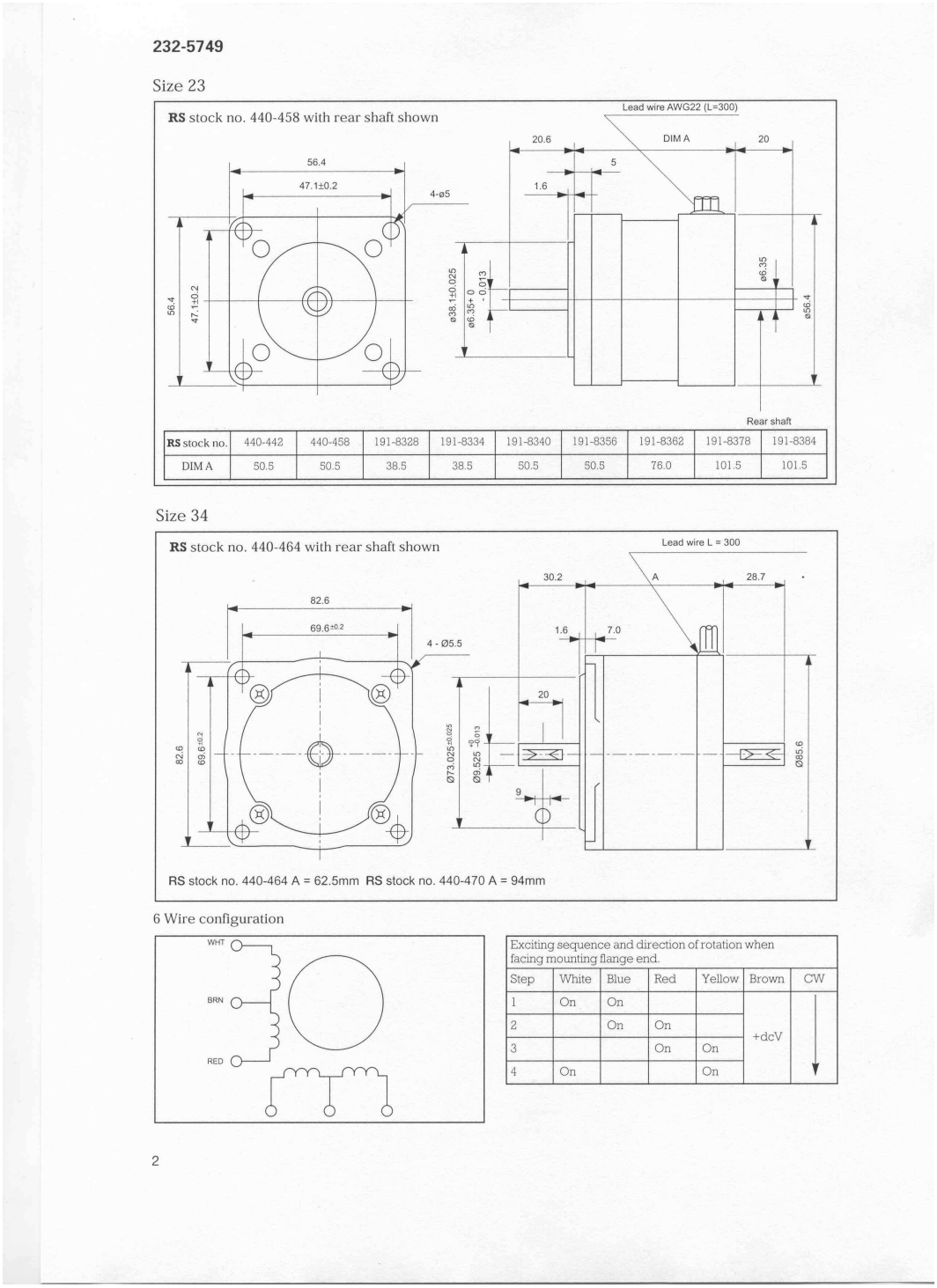

232-5749

Size 23

RS stock no. 440-458 with rear shaft shown

RS stock no.	440-442	440-458	191-8328	191-8334	191-8340	191-8356	191-8362	191-8378	191-8384
DIM A	50.5	50.5	38.5	38.5	50.5	50.5	76.0	101.5	101.5

Size 34

RS stock no. 440-464 with rear shaft shown

RS stock no. 440-464 A = 62.5mm RS stock no. 440-470 A = 94mm

6 Wire configuration

Exciting sequence and direction of rotation when facing mounting flange end.

Step	White	Blue	Red	Yellow	Brown	CW
1	On	On			+dcV	↓
2		On	On			
3			On	On		
4	On			On		

2

Figure B.7: The datasheet of the stepper motor used to drive the linear platform.

232-5749

8 Wire configuration

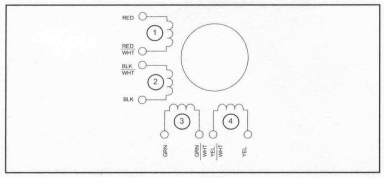

Exciting sequence and direction of rotation when facing mounting flange end.

Step	Red	Green	Black	Yellow	Com	CW
1	On	On			+dcV	↓
2		On	On			
3			On	On		
4	On			On		

Technical specification

RS stock no.	440-420	440-436	440-442	440-458	440-464	440-470
Rated voltage (V)	5	12	5	12	3	2.5
Rated current (I)	0.5	0.16	1	0.6	2	4.5
Resistance (Ω)	10	75	5	20	1.5	0.56
Inductance (mH)	6	36	9	32	4.5	2.8
Detent torque (mHm)	5	4	30	30	40	100
Holding torque (mNm)	70	70	500	500	1200	2200
Step angle accuracy (%)	5	5	5	5	5	5
Step angle	1.8	1.8	1.8	1.8	1.8	1.8
Insulation class	B	B	B	B	B	B

RS stock no.	191-8299	191-8306	191-8328	191-8334	191-8340	191-8356	191-8362	191-8378	191-8384
Rated voltage (V)	12	15	5	12	12	12	5.4	3.4	6
Rated current (I)	0.4	0.4	1	0.4	0.48	0.6	1.4	2.85	1.8
Resistance (Ω)	30	45	5	40	25	20	3.8	1.2	3.5
Inductance (mH)	14	22	5.7	40	33	32	6.8	1.5	7.3
Detent torque (mHm)	3.5	3.5	14.8	14.8	29.6	29.6	56.5	77.6	77.6
Holding torque (mNm)	100	100	260	260	494	494	882	1200	1200
Step angle accuracy (%)	5	5	5	5	5	5	5	5	5
Step angle	1.8	1.8	1.8	1.8	1.8	1.8	1.8	1.8	1.8
Insulation class	B	B	B	B	B	B	B	B	B

Resonance

Certain operating frequencies cause resonance and the motor loses track of the drive input. Audible vibration may accompany resonance conditions. These frequencies should be avoided if possible. Driving the motor on the half step mode (see motor drive methods) greatly reduces the effect of resonance. Alternatively extra load inertia and external damping may be added to shift resonance regions away from the operating frequency.

Motor drive methods

The normal way of driving a 4-phase stepper motor is shown in Figure 1.

Figure 1 **Unipolar drive**

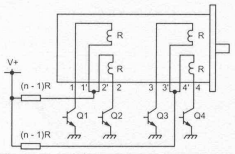

This is commonly known as the 'Unipolar L/nr drive'. Here the current in each winding, when energised, flows in one direction only 'n', value is ≥1 (but not necessarily an integer) and nR is the sum of the external resistance plus the winding resistance (R). By selecting a higher value for n (ie. larger external resistance) and using a higher dc supply to maintain the rated voltage and current for each winding, improved torque speed characteristics can be obtained. Thus a 6V, 6Ω motor (1A per phase) can be driven from a 6Vdc supply without any series resistor, in the L/R mode. Alternatively it can be driven from a 24Vdc supply using 18Ω series resistance in the L/4R mode with much improved performance.

3

Figure B.8: The datasheet of the stepper motor used to drive the linear platform.